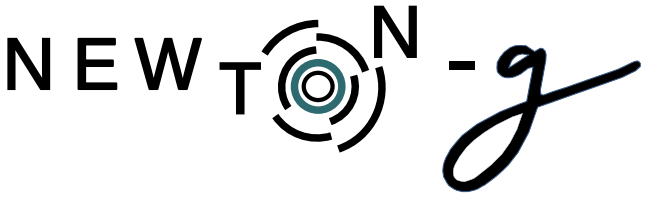

New Tools for Terrain Gravimetry
NEWTON-g
Project number: 801221

Deliverable 4.3

Physical models of relevant processes

Lead beneficiary:	GFZ
Dissemination level:	Public
Version	Final

NEWTON-g has received funding from the EC's Horizon 2020 programme, under the FETOPEN-2016/2017 call (Grant Agreement No. 801221)

Document Information

Grant Agreement Number	801221
Acronym	NEWTON-g
Start date of the project	1 June 2018
Project duration (months)	48
Deliverable number	D4.3
Deliverable Title	Physical models of relevant processes
Due date of deliverable	31 August 2020
Actual submission date	29 September 2020
Lead Beneficiary	GFZ
Type	O: Other
Dissemination level	PU - Public
Work Package	WP4 – Data analysis

Version	Date	Author	Comments
v.0	25/08/2020	Rivalta, Nikkhoo	Creation
v.1	03/09/2020	Rivalta, Nikkhoo	1st revision
v.2	14/09/2020	Rivalta, Nikkhoo, Carbone	2nd revision
Final	29/09/2020	Rivalta, Nikkhoo, Carbone	Validation

Contents

1 Introduction and motivation

Gravity changes at volcanoes may happen due to a number of processes, with or without associated deformation. Examples of such processes are phase transitions in the magma (bubble formation, crystallisation), transport of fluids of different densities (magma, gas, hydrothermal fluids), creation of cracks in the host rock and host rock density change due to elastic strain. These processes may be shallow or deep below the volcanic edifice, they can take place within small or large volume of rock, their source may have different aspect ratios (equi-dimensional or elongated or planar), and may occur over a variety of temporal scales, from seconds to months or years (see Deliverable 3.1). Thus, various temporal scales and spatial patterns are expected to appear in gravity changes measured on the Earth's surface. This is confirmed by observations from volcanoes worldwide; however, the link between underlying processes and observations is often not clear. A number of processes such as those listed above may plausibly act simultaneously, leading to time series of gravity changes difficult to interpret. We illustrate this non-uniqueness in the following, by means of some examples of gravity time series collected by two superconducting gravimeters installed at different elevations and distances to the main craters at Mt. Etna (see Carbone et al., 2019).

As the first example, we consider the time series encompassing the eruptive phase at the beginning of 2017 from the Southeast Crater Complex ("Second Case Study" reported by Carbone et al., 2019, p. 4046–4047). Between 15 and 24 February (phase T1 in Fig. 1), a negative gravity change was observed at both Montagnola (MNT; closer to the summit craters) and Serra La Nave (SLN) stations. The amplitude of the change is much stronger at MNT than at SLN, suggesting the activation of a relatively shallow source. Successively, a three-day gravity increase is observed at both stations (phase T2 in Fig. 1), followed by strong Strombolian activity and lava emission. The value of the MNT/SLN amplitude ratio is smaller during the second phase, suggesting the activation of a deeper source than during the first phase. This is inconsistent with the more intense eruptive activity at the end of T2. Indeed, the gravity increase during the second phase may reflect a more complex process, involving, rather than a single source, mass changes at different depths (e.g., a vertical mass transfer along the conduits feeding the summit craters; see Carbone et al., 2019, for more details).

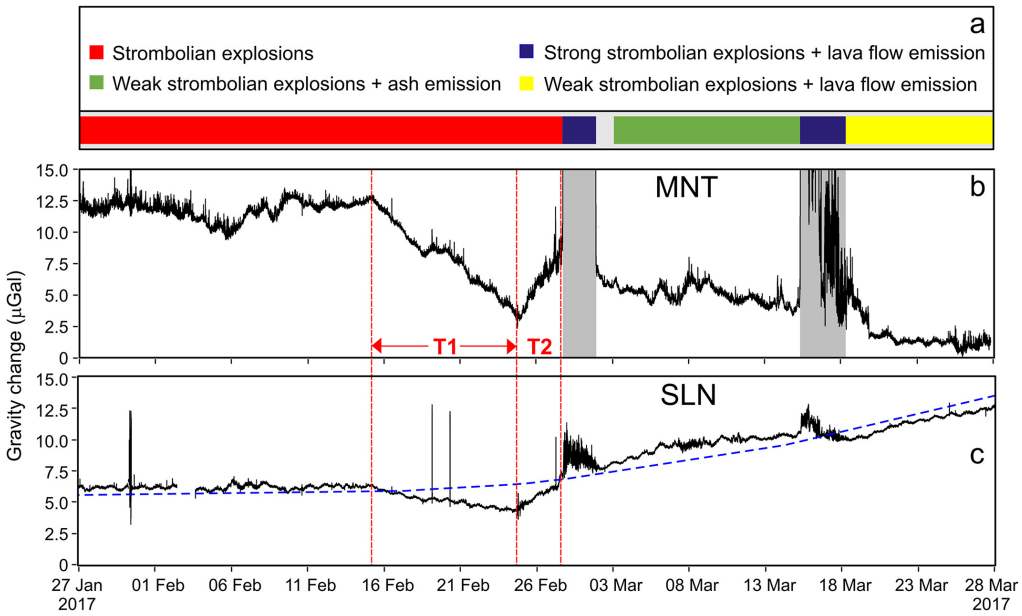

Figure 1: Gravity time series from iGravs on Mt. Etna measured between 27 January and 28 March 2017. (b) Data from MNT, corrected for the Earth tide and local atmospheric pressure and low-pass filtered with cutoff of 10 mHz. Gray stripes mark intervals of severe ground shaking. (c) Data from SLN (same corrections as in b). The dashed blue curve shows the gravity changes driven by underground water-mass redistributions (see Carbone et al., 2017, for details).

As a second example, we present time series of gravity change from MNT and SLN, during mid-May to mid-July 2020. The signals from the two stations are tightly correlated between mid-May and the end of June (see Fig. 2). During this time interval, the almost stable MNT/SLN

amplitude ratio suggests the predominant action of a mass source at fixed depth (likely, 2–3 km below sea level). During the first week of July, a constant-rate increase occurred at SLN, while the signal from MNT displays a more complex pattern, including a decrease between 4 and 6 July, followed by an increase starting on 7 July. Since 9 July, the signal from SLN remained almost stable, while at MNT a sudden drop in the level of the signal occurred on 12 July, followed by a phase of increase. Tese observations suggest that until the end of June only a relatively deep source was active, while, afterwards, the pattern of underground mass changes was more complex. In particular, the opposite sign of the changes at the two stations during early July indicates either the activation of a mass source lying at intermediate level between the elevations of SLN (1740 m) and MNT (2500 m), or the simultaneous occurrence of mass changes at different depths. It is interesting to note that, since the beginning of July, the volcanologists reported resumption of explosive activity at the Southeast Crater Complex.

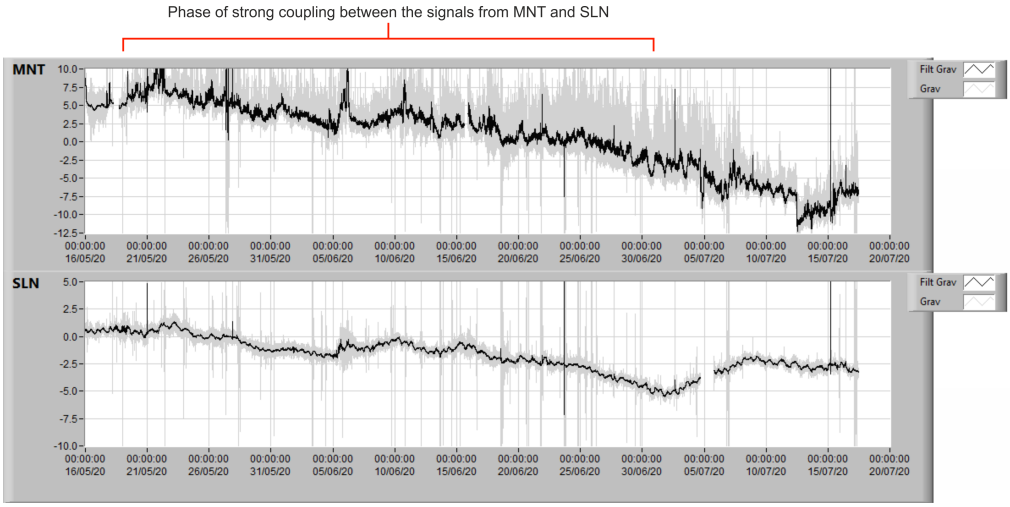

Figure 2: Signals from the iGravs at MNT (top) and SLN (bottom) in the period of time 16 May 2020 to 20 July 2020. See text for more details.

1.1 Scope

The new gravimetric network at Mt. Etna planned in the framework of NEWTON-g is going to provide near-real time information on subsurface mass redistribution with unprecedented spatio-temporal resolution. This opens the possibility to learn more about the processes underlying subsurface mass redistributions, which has not been possible so far due to the lack of continuous and dense gravity observations. In order to better exploit this unprecedented wealth of data, here we focus on process-based physical models for the expected amplitude and pattern, and to some extent time evolution, of gravity changes associated to the most common processes at active volcanoes. We include magma transport by dike propagation, mass input into/output from reservoirs and magma flow in conduits; we extend available solutions to more general source shapes and include magma compressibility. We quantify both the direct gravity change caused by mass redistribution, and the gravity change due to deformation.

2 Common sources of gravity change at Mt. Etna

Mt. Etna is very active. Eruptions occur very frequently and take different forms, including effusive and mildly explosive eruptive activity from the summit craters, and flank eruptions from fissures that open on the flank of the volcano. Beside magmatic activity, the edifice undergoes other processes such as earthquakes, flank motion, diffuse degassing and fluid circulation. Despite these processes often affect small rock volumes, they may cause relatively intense gravity changes since they develop at shallow depths.

2.1 Magmatic sources at Mt. Etna

Magmatic processes at Mt. Etna that may potentially lead to detectable gravity changes (see also Carbone et al., 2017) include propagation and emplacement of dikes (Chauhan et al., 2020), formation of eruptive fissures and lava flows (Branca, 2003; Carbone et al., 2008b), conduit processes feeding lava fountains (Carbone et al., 2015), segregation of bubbles and out-gassing through eruptive vents (Carbone et al., 2008a), accumulation, discharge and convection of magma at a reservoir (Carbone et al., 2003; Carbone and Poland, 2012).

2.2 Tectonic sources at Mt. Etna

Gravity changes may potentially be associated with earthquakes (Branca, 2003) and edifice processes such as seaward motion of the eastern flank of the volcano, which may also lead to creation of voids, seismicity and faulting.

2.3 Hydrological effects

At Mt. Etna, soil moisture and periodic variations of the water table associated with snow melting and rainfall may generate large gravity changes (see Deliverable 4.1). If soil moisture and level of water table are measured, the associated gravity signal can be accurately corrected for. In the absence of such observations, however, we can still filter out the contribution of hydrological effects through analysing the spatio-temporal variations of the gravity signals recorded at a continuously operating network. In the framework of a collaboration with Andreas Güntner from GFZ Potsdam, a number of soil moisture sensors and weather stations will be installed at some gravity sites together with the Micro Electro Mechanical System (MEMS) gravimeters. In the following we assume that the gravity changes of interest are already corrected for hydrological effects.

3 Summary of gravimetric network optimization results for Mt. Etna

The existing gravimetric network at Mt. Etna, composed of three superconducting iGravs, has being augmented in July 2020 with one absolute quantum gravimeter (AQG) and will soon include a network of MEMS gravimeters. AQG-B03 has been installed at the Pizzi Deneri (PDN) Observatory ∼2.5 km from the summit. To find the optimal placement for the MEMS gravimeters we developed a comprehensive optimisation scheme using Genetic Algorithms (Nikkhoo et al., 2020, in preparation). The optimal configuration provides the maximum information content regarding sources of mass change in the target volume encompassing the main locations of magma storage and transport inferred for the past 30 years at Mt. Etna. The scheme is designed to identify the minimum number of MEMS gravimeters needed to reach a given minimum information content for any source of mass change in the target volume. Requiring a coverage level equivalent to that provided by 4 optimally placed MEMS gravimeters for each target source, returned 13 as the minimum number of MEMS gravimeters to complement the two iGravs and the AQG (Fig 3). The sources of mass change in the target volume are assumed to be much farther from the gravimeters than their extent, such that their surface gravity signature can be well approximated by that caused by a point mass. Depending on the distance, this point mass approximation is very accurate for equidimensional sources (e.g. an almost spherical reservoir) and less accurate for elongated (e.g. a conduit) or planar (e.g. a dike) sources.

We assess the point mass approximation quantitatively by applying numerical integration to simple source geometries. These calculations show that the safe distance for a generic cuboid of size a_x, a_y and a_z along the x, y and z axes, respectively, can be defined as a function of the a/d ratio, where a is the largest side of the cuboid and d is the depth to the centroid. The point mass approximation results in a relative error well below 5 per cent if $a/d \leq 0.8$ for a cube $\{a = a_x = a_y = a_z\}$, $a/d \leq 0.6$ in case of a thin vertical plate $\{a = a_y = a_z,\ a_x \ll 1\}$, $a/d \leq 0.4$ in the cases of both a thin horizontal plate $\{a = a_x = a_y,\ a_z \ll 1\}$ and a thin vertically-elongated volume $\{a = a_z,\ a_x = a_y \ll 1\}$.

A network optimised according to the scheme by Nikkhoo et al. (2020) is fit to locate any point mass located within the target volume that generates a detectable gravity change at a minimum of four stations of the network. Such network can also be used to image a more extended mass

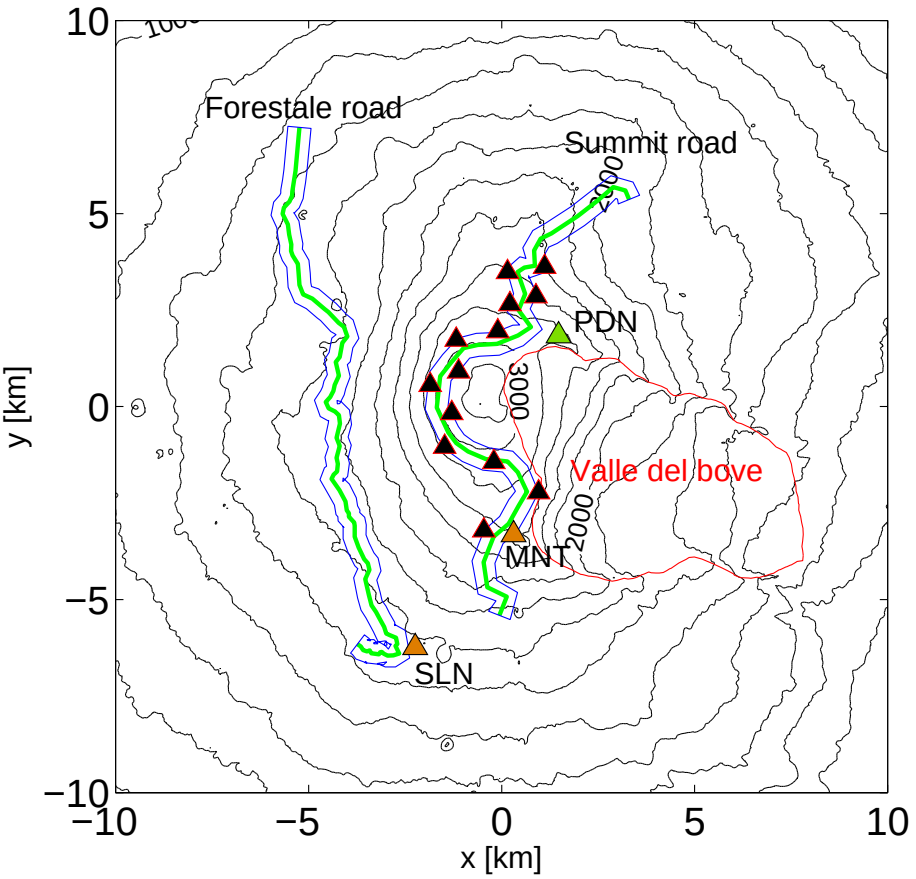

Figure 3: The optimal network configuration for the MEMS gravimeters (black triangles) at Mt. Etna. The green and orange triangle at PDN, MNT and SLN indicate the AQG and two iGrav superconducting gravimeters that are all currently operational. The blue lines mark the 600 m strips centered on each road.

redistribution in the target volume, provided that the sources generate a signal above the signal-to-noise ratio (Hardt and Scherbaum, 1994).

4 Gravity changes due to mass transport and associated deformation

4.1 Coupling between deformation of the host rock and gravity changes

Mass transport changes the gravity field both directly, that is due to the added or removed mass, and indirectly, through deforming the host rock, as follows (e.g. Walsh and Rice, 1979; Okubo, 1991, 1992; Segall, 2010, Ch. 9.5): 1) Displacement of the Earth's surface shifts the gravimeters vertically away from the centre of the Earth, thereby changing the gravity readings by an amount that is referred to as the "free-air" effect; 2) Displacement of the Earth's surface also adds a layer of rock between the previous and the current Earth's surface, thus changing the gravity; 3) Dilatational and compressional strains in the host rock also change the gravity field through local density changes. Surface deformation can be measured reliably with geodetic techniques such as GNSS (Global Navigation Satellite System), SAR (Synthetic Aperture Radar), precise levelling or other ground-based approaches. Thus, using observations of the vertical displacement at the gravity sites, the free-air effect can be accurately removed from the observations. The free-air effect, Δg_{FA}, can be calculated through

$$\Delta g_{\text{FA}} = \gamma u_z \doteq -308.6 u_z, \tag{1}$$

where u_z is the vertical displacement at the gravity site, γ is the free-air gradient (e.g. Segall, 2010, p. 284). In eq. 1 Δg_{FA} is in µGal if u_z is given in meters.

Correcting for effect number 2 ideally requires dense observations of vertical displacement of the Earth's surface around the sites. However, the Bouguer correction in most cases, especially for mild topographies, approximates effect number 2 fairly well. This correction can be calculated as

$$\Delta g_{\text{B}} = 2\pi G \rho u_z, \tag{2}$$

where Δg_{B} is the Bouguer correction and ρ is the density of the host rock. For a density of $\rho = 2670\,\text{kg}\,\text{m}^{-3}$ we have $\Delta g_{\text{B}} = 111.9 u_z$ µGal m^{-1}.

Correcting for effect number 3, in contrast, requires knowledge of the subsurface volumetric strains induced in the host rock, which cannot be directly observed. A model of the deformation induced by mass transport is needed to correct for effect number 3. If such a model is available, then effects number 1 and 2 can also be estimated.

While deformation alters gravity, the pattern of pressure changes does not coincide entirely, in general, with the pattern of mass changes. For example, a dike may be pressurised due to the buoyancy of its magma, so that both pressure distribution and mass change overlap spatially within the dike. However, due to such pressurisation the dike also compresses rock at its side and extends it around its tipline, moreover the Earth's surface above the dike and at its sides will subside and be uplifted, respectively. Due to this lack of spatial correspondence, and ultimately due to the fact that elasticity and gravitation behave differently, as explained in more detail below, deformation and gravity observations are in general difficult to reconcile.

The deformation field is determined by the pressure distribution on the pressure source walls and by the elastic properties of the medium, which dictate the reaction of the host rock to pressurisation. Thus, for the purpose of calculating the induced deformation, we can approximate the body as a cavity of similar shape. In other words, the deformation field is blind to processes occurring in the fluid contained in the source, unless they affect the pressure distribution on the reservoir walls. If pressurisation occurs, the pressure distribution and in turn the shape of the body will determine the deformation field. As long as the induced ground deformation is large enough to be detected at the Earth's surface, the effect of the body shape will be seen in the signal, as the pattern for different shapes looks very different. In contrast, gravity changes are determined by the distribution of mass changes in the medium. As seen above, we need to account for the direct effect of any intruded or displaced mass and for the indirect effects arising from the deformation of the medium. Regarding the direct effects, if the volume of rock affected by mass change has a large distance to the gravimeters compared to its lateral size, it can be treated as a point source, meaning that regardless of its shape the gravity change will be similar to that due to the same mass change concentrated in a single point, or equivalently, in a sphere of any radius. Only in the near field the shape of the mass change distribution matters. However, as introduced above, the gravity change is coupled to the deformation in different ways and requires a deformation model to be calculated.

Analytical expressions for the deformation and stress field induced by pressurisation of cavities in elastic media have been used extensively to infer the unknown parameters of deformation sources (Segall, 2010). Recently, Nikkhoo et al. (2017) proposed a generalised source, the compound dislocation model (CDM), which can be set to be equivalent to most individual shapes for which an analytical solution exists.

More flexible numerical calculations have allowed to include topography or layering (e.g. Bonaccorso et al., 2005) or more complicated medium rheologies (e.g. Currenti, 2018) in the calculations.

4.2 Time scales of some important magmatic processes

We revised the time scales over which gravity changes due to different volcanic processes occur in Deliverable D4.1.

Dike propagation have typical velocities of $1\,\text{km}\,\text{h}^{-1}$ but may accelerate, decelerate or stop on their way due to internal (e.g. vesiculation or outgassing varying the magma density and viscosity) and external (e.g. medium heterogeneities, free surface, sudden external forcing such as earthquakes or tidal loading) factors.

As an example, dikes at Mt. Etna have been observed to stop as an intrusion, or accelerate and erupt, or slow down and propagate laterally before reaching the Earth's surface. Available models can only roughly explain such dynamics a posteriori, as resulting from a number of contributions

such as stress field (flank dynamics, previous dikes, topography). Such models still lack predictive power. Other processes including phase changes, which have dramatic effects on gravity change, are even more challenging to predict.

The same is true for magma reservoirs and conduit processes. The speed of flow of magma in a conduit can vary over several orders of magnitude and undergo accelerations depending on a large number of parameters. The velocity at which magma density evolves in a magma chamber does also depend on a large number of factors as scenarios may vary depending on the volumes of newly input magmas, their composition, the composition and physical properties of the magma pre-existing in the reservoir, reservoir permeability, heat conduction and advection, among many others (see e.g. Jackson et al., 2018).

Therefore in what follows we do not restrict the models to have any specific time history. We model scenarios as a series of snapshots that can be then converted into a proper time series by assuming a user-defined "source time function".

4.3 Our approach for deformation and gravity change calculations

To calculate the deformation field associated with planar dikes, faults and pressurised cavities, we use analytical solutions such as rectangular dislocations (RDs; Okada, 1992; Nikkhoo et al., 2017) and point spherical source of pressure Mogi (1958) and case-by-case extended to more general sources by using the compound dislocation model (CDM; Nikkhoo et al., 2017). This way we can model pressurised cavities of planar, cylindrical and ellipsoidal shape as a set of one, two and three orthogonal RDs (see Fig. 4), respectively. The surface displacement and the underground strain field will feed back into the gravity calculations. In order to simulate dike propagation we also use crack models, where we discretise the dike into many RDs and prescribe their opening to match that of the analytical solution for a three dimensional penny-shaped crack in a full space. For gravity change, we make use of the Okubo (1991, 1992) models and the MATLAB code developed by Beauducel (2012) to calculate the total gravity changes associated with the CDM.

5 Dike propagation

5.1 Dike dynamics with focus on Mt. Etna

Diking is the main mechanism through which magma is transported from deep levels, where melt is produced, to the Earth's surface. Dikes are thin, often vertical, sheets of magma that propagate by hydraulic fracturing. Most "freshly intruded" and eroded dikes at Mt. Etna are from 0.3 to a few meters thick, and are a few kilometers wide and long. Dikes may stall on their way as intrusions or feed reservoirs at intermediate levels. Once reservoirs are pressurised, they may also nucleate dikes, thereby partly draining and depressurising. Only a fraction of the dikes that propagate below volcanoes eventually reach the Earth's surface to erupt. When they do, they create eruptive fissures, from which lava is emitted as a curtain of fire. In the past 30 years, dikes at Mt. Etna have propagated sub-vertically towards the summit area at velocities of the order of $1\,\mathrm{km\,h^{-1}}$ (e.g. Aloisi et al., 2020), and have erupted along the North and South rifts or in the Valle del Bove, sometimes after a change of propagation direction from vertical to horizontal. Dikes may both accelerate or slow down along their path, due to a number of velocity-boosting (bubble nucleation, closeness to the free surface, becoming more vertical) and velocity-reducing (degassing, encountering rock layers where they become anti-buoyant, becoming more tilted or curved) processes. Detailed observations of such increasing or decreasing velocities are not available for Mt. Etna, although observations of dikes that first ascend vertically before turning to lateral propagation are very common (Wright et al., 2012; Thiele et al., 2020).

5.2 Simple models for dike-induced deformation

The deformation field induced by a dike can be calculated by using models of pressurised cracks or tensile dislocations. A penny-shaped crack is the simplest example of a pressurised crack. It is a circular crack subjected to a prescribed pressure (often uniform pressure) on its walls. This results in a non-uniform opening over the crack walls, depending on the boundary condition; the aperture of a two-dimensional crack is elliptical for uniform pressure (Fig. 5, top) and tear-drop shaped for a linear pressure profile. In contrast, tensile dislocations use displacement boundary

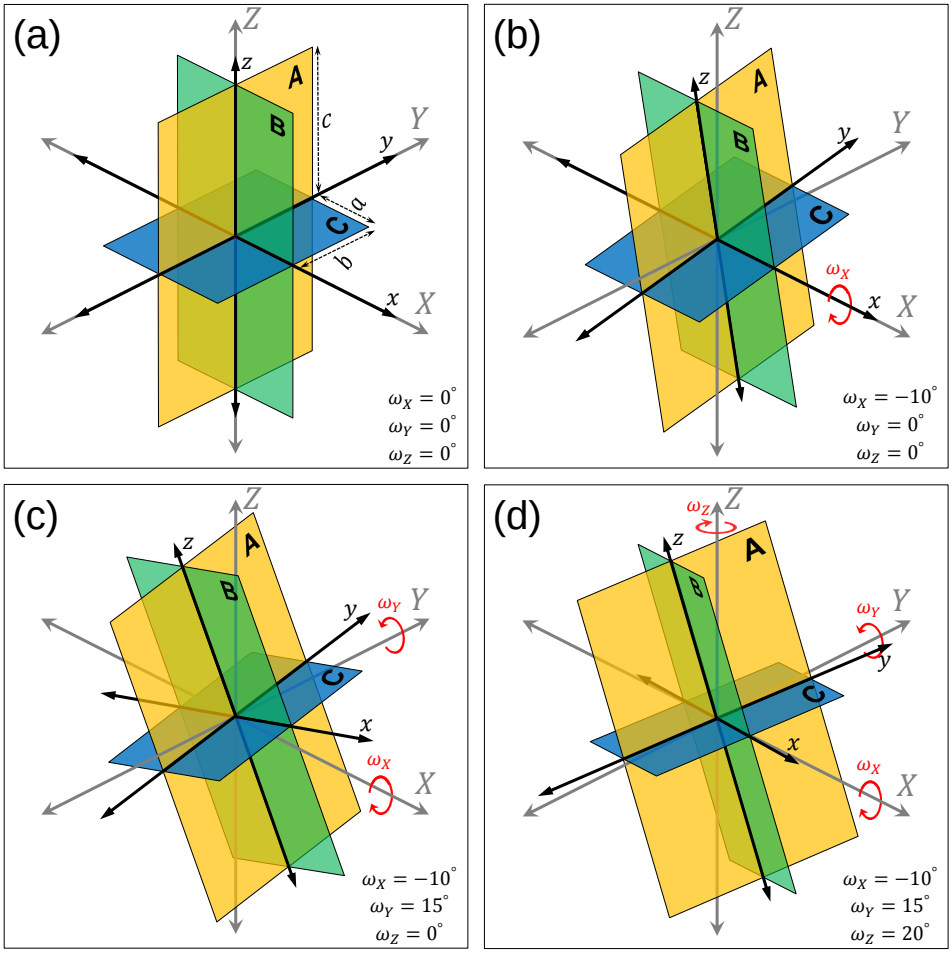

Figure 4: The structure of the CDM composed of three orthogonal RDs (the yellow, green and blue planes), labelled as 'A', 'B' and 'C'. The XYZ coordinate system is Earth-fixed and the xyz coordinate system is fixed to the CDM. The ωX, ωY and ωZ are angles of rotation about the X, Y and Z axes, respectively. Examples of a CDM with the semi-axes a, b and c along the x, y and z axes, respectively, and different rotation angles are illustrated in panels a-d. The rotation angles in each case are indicated on the bottom right of each panel. Fig. 3 from Nikkhoo et al. (2017).

conditions, for example uniform opening of the dislocation surfaces (Fig. 5, bottom). These models are equivalent in the far-field, that is large distances compared with the dimension of the dike, but show some differences in the near field.

5.3 Volume, aspect ratios, 3D shape of dikes

While much larger "frozen" dikes are observed in the field around the world, dike intrusions that have occurred since modern monitoring systems are in place have not exceeded a few km^3, with only a handful dikes exceeding 1×10^8 m^3. Over the past 40 years, the volume of dikes at Mt. Etna has been from a few to a few tens of millions m^3 (Bonaccorso et al., 2017). The lateral size of these dikes has ranged from almost one to a few kilometers, and the opening was from about half a metre to a few metres.

From a theoretical point of view, the aspect ratio and the 3D shape of dikes varies according to the elastic parameters of the host rock, the gradient of stress driving the dike, and a parameter called "fracture toughness", which describes the energy needed to fracture the host rock to advance the dike. For vertically propagating dikes the driving gradient is determined by the difference of density between the rock and the magma. For laterally propagating dikes, the driving gradient is mainly controlled by the topography gradient along the dike path (e.g. Urbani et al., 2017). Host rock layering (density and rigidity) interacts with all these factors to determine the 3D shape of a dike and the induced strain field. For example, a vertical buoyant dike theoretically assumes a tear-

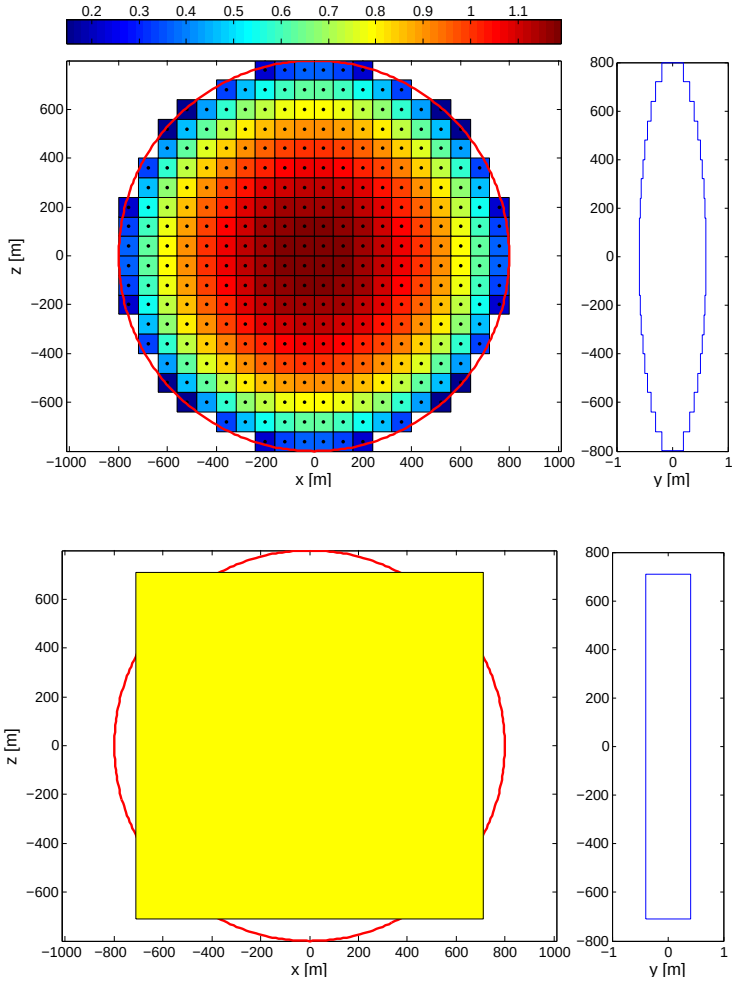

Figure 5: Top left: Front view of a mesh of 316 RDs simulating a vertical penny-shaped crack (red circle) of volume $1.6 \times 10^6\,\mathrm{m}^3$ (a small dike at Etna). The color indicates the opening of the RDs. Top right: Side view of elliptic opening of the penny-shaped crack. Bottom left: An RD with the same area and volume as the penny-shaped crack. The red circle is for comparison. Bottom right: Uniform opening of the RD is a mean value of the opening on the penny-shaped crack walls.

drop shape (Weertman, 1971). However, usually host rock density decreases towards the Earth's surface, making the upper part of the dike anti-buoyant and thus thinner (Taisne and Jaupart, 2009). A model considering all these interacting effects would necessarily be very complex and require long calculations, beside containing many epistemic uncertainties. We therefore consider simple rectangular dislocations as appropriate models for dikes for the present aims. For the sake of comparison and to estimate near-field errors incurred with such simplifications, we also present simple models of dikes shaped as penny-shaped cracks in a full space (Fig. 5).

5.4 Dike propagation speed

Dikes propagation speed in the upper crust may range from a fraction to a few $\mathrm{km\,h}^{-1}$. From a theoretical point of view, dike speed varies according to the gradient of stress driving the dike, to its volume and to the viscosity of the magma. At Mt. Etna, given that density and viscosity of magmas do not vary much (Corsaro and Pompilio, 2004), this would translate into a dependence on dike strike and dip (affecting the vertical stress gradient) and volume. Dike speed may be observed directly from the propagation of fissures or fractures during emplacement, or indirectly from deformation (time-dependent inversions of dike geometry) or seismicity (tracking the seismicity clustering around the dike tip), but not many detailed observations are available at Mt. Etna to estimate any increase or decrease in the propagation velocities of dikes along their pathways.

In spite of new developments in forecasting the pathway and velocity of propagating dikes

(Sigmundsson et al., 2015; Pinel et al., 2017; Rivalta et al., 2019), reliable models tailored for a specific volcano are not available, so we model dike propagation by shifting the rectangular dislocation (or the crack composed of several rectangular dislocations) by the same distance step after step. With limited work, it is straightforward to define a time-dependent velocity on a prescribed curved pathway as preferred. This corresponds to convolving our solutions to a predefined "source time function". The volume of the dike can also be changed along its pathway, if desired.

5.5 Scenarios of deformation and gravity change due to diking, with application to Mt. Etna

As it occurs with other bodies, a dike intrusion affects gravity by changing the density distribution in the host rock in the following ways: 1) it substitutes host rock with magma within the volume occupied by the dike, 2) it displaces the gravity stations by deforming the Earth's surface, 3) it strains the underground thereby changing the density of the host rock locally. All these contributions can be estimated separately by using the model by Okubo (1992).

First, we will examine the gravity change caused by the creation of a cavity of the shape of a rectangular dislocation (sides of 3 km and opening of 1 m) without any mass input (Fig. 6a-f). The expected gravity change before any correction is dominated by the free-air component (Fig. 6a), and to some lesser extent, by the effect of mass redistribution at the Earth's surface, seen in Fig. 6e. The latter effect is similar to the Bouguer correction except that it is carried out by integrating the real surface displacement and not a layer of constant thickness. If both the free-air and the "Bouguer" components are removed, we obtain the map seen in (Fig. 6b), which shows very clearly the creation of a cavity. This elongated pattern does not result from the elongated dike-shaped cavity, rather it is the superposition of the direct mass removal effect (Fig. 6d) and the volumetric strain induced in the host rock, that is, contraction at the dike's sides and dilatation all around its tipline (Fig. 6f).

Next, we consider the case that the cavity created by the RD is filled with buoyant magma of density 2400 $\mathrm{kg\,m^{-3}}$, that is, 300 $\mathrm{kg\,m^{-3}}$ less than that of the host rock (see Fig. 7a-f). Panels a, c, e and f remain unvaried with respect to the cavity case above, as they all result from the same deformation. Panels b and d appear extremely different as now there is no cavity. The overall gravity change is very small and almost entirely resulting from volumetric strains in the rock. The direct effect is small and negative, because the intruded magma density is lower than that of the host rock. The minimum gravity change is associated with the case that the cavity is filled with neutrally buoyant magma of density equal to that of the host rock. In such a case the direct effect is zero and the overall gravity change is entirely resulting from the volumetric strains in the host rock.

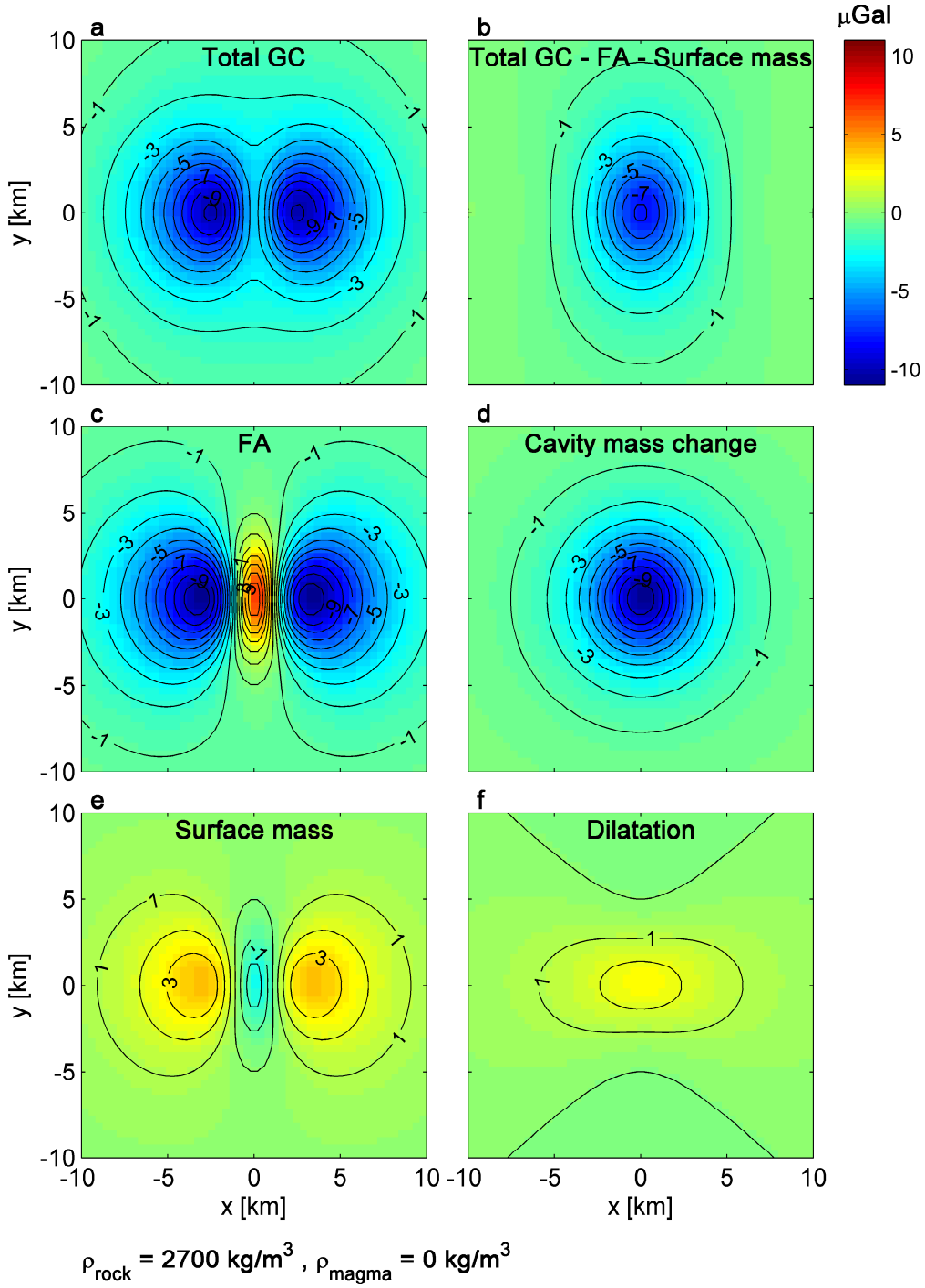

Figure 6: Gravity changes due to the opening of a 3×3 km tensile RD with a centroid depth of 4 km. The opening of the RD is 1 m and the density of the host rock is 2700 kg m^{-3}. a) The total (observed) gravity change, b) The gravity change after correcting for the free-air gradient and the surface mass redistribution effects, c) The free-air contribution, d) The cavity contribution, e) The contribution of the surface mass redistribution, f) The contribution of the dilatation field.

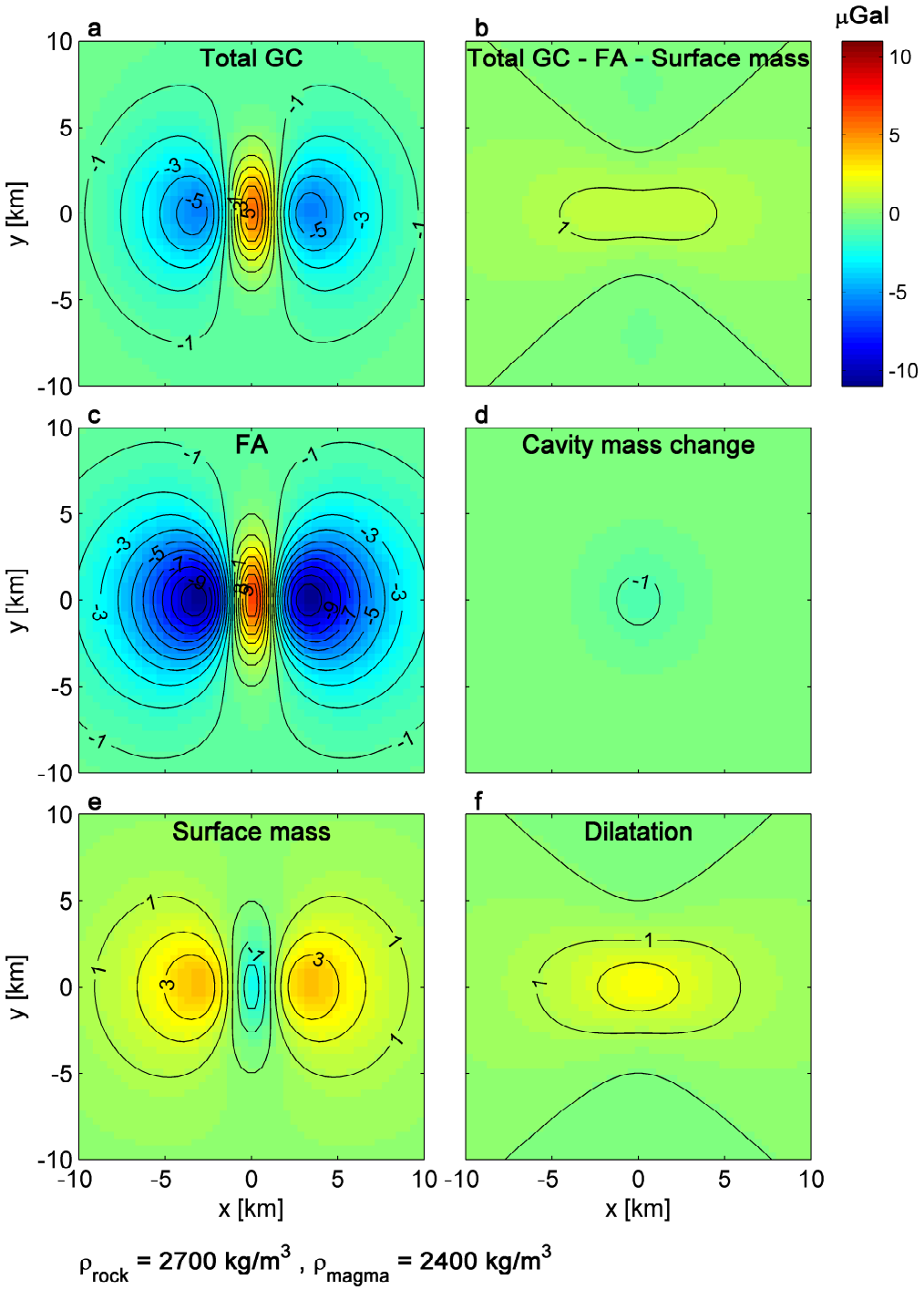

Figure 7: Gravity changes due to the opening of a vertical 3×3 km tensile RD with a centroid depth of 4 km. The opening of the RD is 1 m, the density of the host rock is 2700 kg m^{-3} and the density of the magma filling the dislocation is 2400 kg m^{-3}. a) The total (observed) gravity change, b) The gravity change after correcting for the free-air gradient and the surface mass redistribution effects, c) The free-air contribution, d) The cavity contribution, e) The contribution of the surface mass redistribution, f) The contribution of the dilatation field.

From these figures it is evident that correcting for free air and Bouguer, either directly from GNSS data or from deformation models, is fundamental to correctly interpret the pattern of gravity changes due to dikes. It also shows how neutrally buoyant dikes may result in extremely low gravity changes. Dikes at Mt. Etna can be 20 times more voluminous than what examined.

Next, we compare the gravity changes (total gravity changes and those with free-air and Bouguer removed) caused by a dike shaped as a square dislocation and one as a penny-shaped crack of the same volume as above and filled with a magma with density 2400 kg m^{-3}, as measured by gravimeters placed on a profile perpendicular to the dike at its centre. Differences become relatively large only when the dike is very close to the Earth's surface (Fig. 8); such differences would increase if the profile was measured off from the centre of the dike.

As a final comparison, we show the "time series" for a dike approaching the free surface (Fig. 9) as measured by the stations determined by the network optimization, except that they all lie on a flat surface 2800 m above sea level instead of on the real topography of the volcano. The dike is centered on a vertical line through the summit and strikes NS. Since we take vertical steps of the same size for the dike, these "time series" would apply to a dike that does not change its aspect ratio and approaches the free surface at constant velocity. The simple models used here cannot be used to also consider the elevation of the stations, this requires a numerical model that accounts for the effects of the topography on the surface displacement resulting from dike opening, as we saw these dominate the total gravity change and need to be calculated accurately (e.g. Currenti et al., 2007). The modelled values of gravity change do not exceed 10 µGal and 3 µGal for the total and corrected values, respectively. Thus, most dikes at Etna may be seen by the future network as the one we modelled is on the lowest end of the size range observed in the last 40 years.

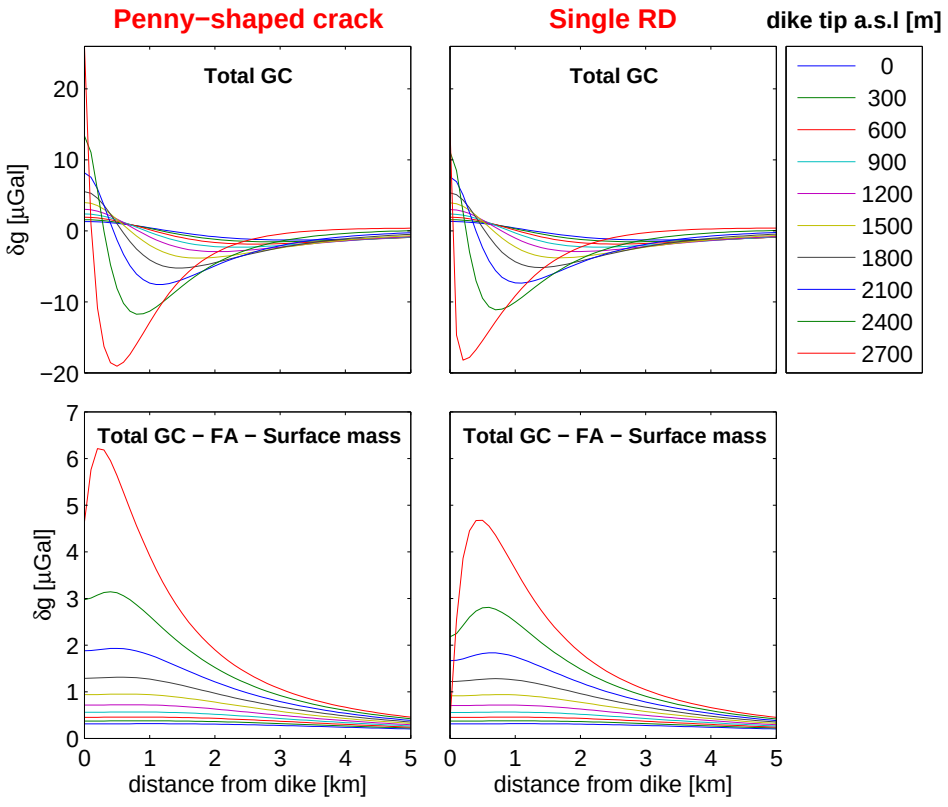

Figure 8: Surface profiles of gravity changes for stations aligned perpendicular to an ascending dike. The elevation of the Earth's surface is 2800 m in the simulations. Different lines correspond to different snapshots (every 300 m) during the ascent. The left and right columns are for a penny-shaped crack and for an RD, respectively. The upper row is for total gravity changes, while the lower row is after free-air and Bouguer corrections.

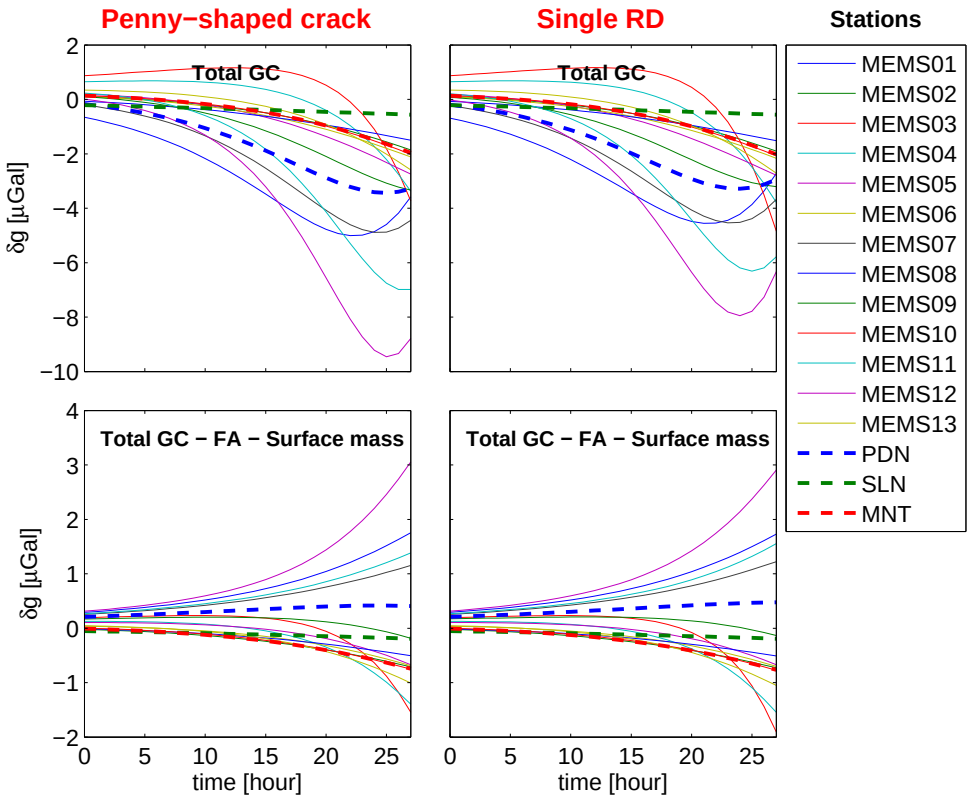

Figure 9: Gravity change time series for the optimised MEMS stations (Fig. 3), except they lie on the surface of a half-space at an elevation of 2800 m. Different lines correspond to different stations, as explained in the inlet. The left and right columns are for a penny-shaped crack and for an RD, respectively. The upper row is for total gravity changes, while the lower row is after free-air and Bouguer corrections.

6 Reservoirs

At many volcanoes, geophysical methods have revealed the existence of one or more reservoirs of various sizes and geometries. Reservoirs have been detected in different ways: as heterogeneities in seismic wave velocities revealed by tomography (Koulakov et al., 2013), as regions of anomalous electric conductivity, as rock volumes from which some pressurisation over lithostatic levels acts to bulge the overlying rock layers (e.g. Segall, 2010), as rock volumes which undergo mass change, as depths where the composition of magma evolves towards geochemical equilibrium. In general, all these regions identified with different techniques are difficult to reconcile with each other; the challenge holds even if we consider only deformation and gravity changes.

Two main basic scenarios come to mind when considering gravity changes associated with reservoir processes: 1) the reservoir's infill mass increases through inflow of new mass or decreases through outflow of some mass from the reservoir; 2) the infill mass remains constant but the density distribution changes, e.g. due to nucleation, growth and upward migration of bubbles. The magnitude and pattern of gravity changes associated with these basic processes are still poorly understood. Here we address these two scenarios by extending previously obtained analytical results for spherical reservoirs to more general shapes. We first summarise both published analytical results for spherical geometry and numerical results for some ellipsoidal geometries. Next, we develop semi-analytical solutions to model deformation and gravity change scenarios involving ellipsoidal sources of any aspect ratio, and show how these models can be used to interpret observations of ground deformation and gravity change.

6.1 Previous analytical results for spherical magma reservoirs

The most basic way to model deformation and gravity changes at reservoirs is to adopt an isotropic point source or spherical cavity. If the radius a of the cavity is much smaller than its depth d, then the displacement components on the surface are (e.g. Okubo, 2020):

$$\mathbf{u}(u_r; u_\theta; u_z) = \frac{(1-\nu)\delta p}{\mu} \frac{a^3}{(r^2+d^2)^{3/2}} (r; 0; d), \tag{3}$$

where r, θ and z are the coordinates of a cylindrical system with origin over the spherical cavity, δp is the pressure change, and μ and ν are rigidity and Poisson's ratio of the medium, respectively (Yamakawa, 1955). Alternatively, eq. 3 can be written in terms of magma reservoir volume change:

$$\delta V = \pi \delta p a^3 / \mu \tag{4}$$

obtaining:

$$\mathbf{u}(u_r; u_\theta; u_z) = \frac{(1-\nu)}{\pi} \frac{\delta V}{(r^2+d^2)^{3/2}} (r; 0; d) \tag{5}$$

(see also Segall, 2010, eqs. 7.14 and 9.75).

Following the scheme proposed by Okubo (1992, 2020), the surface gravity change Δg measured at a point solidly connected to the ground comprises the following four contributions: (1) the free-air gravity change, Δg_{FA}, due to the uplift of the observation point; (2) the attraction of the surface mass redistribution (single layer), Δg_{SL}, originating from the deformed ground; (3) the attraction from the perturbed density field, Δg_{DF}; and (4) the direct attraction of the mass transported to/from the magma reservoir, Δg_{DIR}.

Walsh and Rice (1979) demonstrated that for a spherical cavity in a homogeneous half-space $\Delta g_{\text{SL}} = -\Delta g_{\text{DF}}$, that is, the surface gravity change residual after free-air correction vanishes. This means that any gravity change measured above a spherical chamber and corrected for free-air contribution must originate from mass input/output δM. If the source is isotropic, the spatial shape of the deformation functions in eqs. 3 and 5 coincide with the spatial shape of the gravity change function (Newton equation). Combining eqs. 1, 5 and the Newton equation results in:

$$\Delta g - \gamma u_z = G \delta M \frac{d}{(r^2+d^2)^{3/2}} \tag{6}$$

(e.g. Segall, 2010, p. 284). At this point, one can eliminate the spatial function in eq. 6 by using eq. 5 to obtain:

$$\frac{\delta M}{\delta V} = \frac{(1-\nu)}{\pi G} \left(\frac{\Delta g}{u_z} - \gamma \right). \tag{7}$$

The gradient $\Delta g / \Delta h$ on the right-hand-side of eq. 7 has been the focus of many studies (Eggers, 1987; Rymer and Williams-Jones, 2000; Gottsmann et al., 2003), which attempted to link it to the underlying process and forecast future volcanic activity scenarios. This approach is based on the assumption that the magma reservoir is spherical; as shown by (e.g. Currenti et al., 2007) and Trasatti and Bonafede (2008) interpretation may be incorrect if the magma reservoir has a different aspect ratio. The ratio $\Delta g / \Delta u_z$ should be constant over the network for a spherical chamber, while significant deviations are expected for other geometries (see additional caveats in Johnson, 1992; Segall, 2010, p. 292).

Note that $\delta M / \delta V$ from eq. 7 is not the density of the intruded material because the volume change of the reservoir δV is in general smaller than the volume of the intruded material. This is because the intruded material deforms a magma reservoir in two ways: A) by pushing the reservoir walls outwards and B) through compressing the material already stored in the reservoir (Fig. 10). δV only reflects contribution **A**. The relative size of zones **A** and **B** in Fig. 10 depends on the reservoir shape and on the ratio of host rock compressibility to magma compressibility. If the magma is bubble-free, for a spherical magma reservoir zones **A** and **B** will have comparable sizes.

6.2 Effects of magma and host rock compressibility

Gravity changes accompanied by a lack of deformation have been observed in several instances (e.g. Carbone et al., 2003; Johnson et al., 2010; Poland et al., 2019). Similarly, other works report large

gravity changes accompanied by rather small deformation (Bagnardi et al., 2014). Void formation and filling, which lead to gravity changes with no deformation, have been often proposed to explain this kind of observations (Eggers, 1987). Poland et al. (2019) observed a phase of gravity changes with lack of deformation at Kilauea, Hawai'i, followed by a phase where deformation gradually took up. They interpreted this observation as filling of voids that eventually led to the reservoir pressurisation. Void filling has not yet been thoroughly addressed in terms of gravity changes from a theoretical point of view.

Magma compressibility and rock elasticity are important factors to consider when linking magma chamber processes to observed gravity changes. Compressibility links the pressure changes to density and volume changes directly and its effects may result in large apparent volume discrepancies (e.g. Rivalta and Segall, 2008). In the next sections, we examine the role of magma compressibility in inducing gravity changes.

6.2.1 Fluid intrusion into a reservoir

Assuming that the density of the intruded fluid, ρ, is the same as the fluid already contained in the reservoir (same compressibility of the liquid phase and same gas phase fraction) pressure will increase according to the following equation (e.g. Segall, 2010):

$$\delta M = \delta(\rho V) = \rho \delta V + V \delta \rho = \rho V(\beta_m + \beta_c)\delta p, \tag{8}$$

where

$$\beta_m = 1/\rho(\,\partial\rho/\partial p\,) = 1/K_m, \tag{9}$$

with K_m magma bulk modulus, is magma or hydrothermal fluid compressibility (its relative density variation as a function of pressure), and

$$\beta_c = 1/V(\,\partial V/\partial p\,) \tag{10}$$

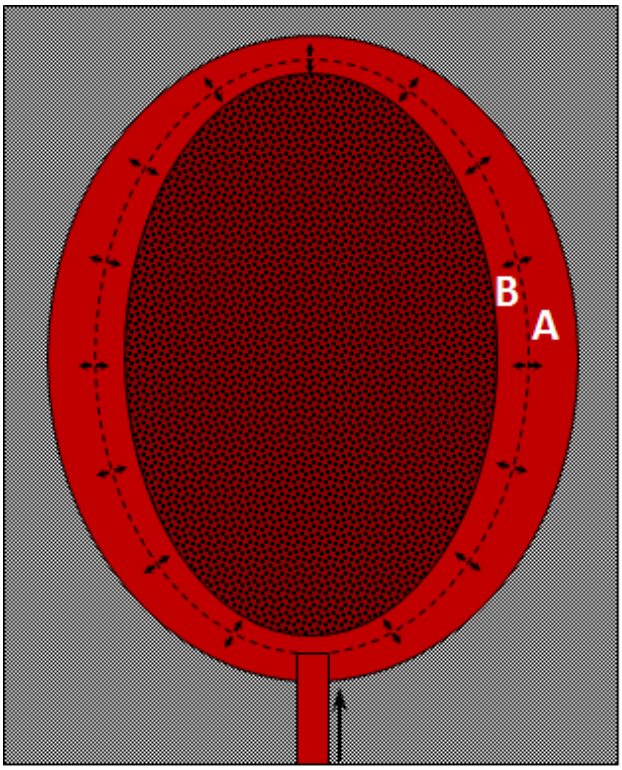

Figure 10: The dashed line illustrates the reservoir boundary before intrusion. After intrusion the reservoir boundary is pushed outwards (external solid line). The volume created by the compression of host rock is zone A, while compression of the material already stored in the reservoir (zone B) accommodates the rest of the intrusion volume.

is the compressibility of the reservoir due to medium elasticity and reservoir shape (relative volume change as a function of pressure). For a spherical reservoir, eq. 4 leads to $\beta_c = 3/(4\mu)$. We can also substitute $V\delta p$ with $\delta V/\beta_c$ in eq. 8 to have:

$$\delta M = \rho \left(\frac{4\mu\beta_m}{3} + 1 \right) \delta V. \tag{11}$$

Thus

$$\frac{\delta M}{\delta V} = \rho \left(\frac{4\mu\beta_m}{3} + 1 \right), \tag{12}$$

from which the density of the material can be calculated if β_m is known. Note that ρ needs to be consistent with β_m, because they are not independent but linked through eq. 9. We note that eqs.11 and 12 are only valid for spherical reservoir geometry (Johnson, 1992; Segall, 2010).

6.2.2 Fluid extrusion from a reservoir

Above we considered intrusion into a magma reservoir from below; a slightly different case is a magma reservoir feeding an intrusion or an eruption. Sometimes it is possible to estimate from ground deformation and other field data both the reservoir volume loss and the volume gained by the dike, or the erupted volume. When this is the case we have the opportunity to estimate magma compressibility directly from observations, rather than assuming a theoretical value.

Following many workers (Johnson, 1992; Johnson et al., 2000; Mastin et al., 2009), Rivalta and Segall (2008) and Rivalta (2010) related the ratio between a dike's volume V_d and the volume change δV at the reservoir feeding the dike, to magma and chamber compressibility as follows:

$$V_d/\delta V = r_V = 1 + \frac{\beta_m}{\beta_c}. \tag{13}$$

This equation rationalises the common observation that dike volumes, or alternatively erupted volumes, are larger than the volume loss at the reservoirs feeding them (Rivalta and Segall, 2008; Kilbride et al., 2016). This can then be used to constrain the fluid density by using it within eq. 12:

$$\rho = r_V^{-1} \frac{\delta M}{\delta V} \tag{14}$$

In several dike injection or eruption cases, β_m remained stable during the injection or eruption. Examining time-dependent volume change inversions from ground deformation for the 2000 intrusion at Miyakejima, Japan, Rivalta (2010) observed that r_V remained constant over a time span of at least 12 hours during the intrusion process. Hreinsdóttir et al. (2014) found that β_m remained constant in the reservoir also for the 2011 explosive eruption of Grimsvötn, in spite of the massive exsolution of gas, which therefore must then have occurred at shallower depth, while the magma infilling the reservoir remained at the original density.

If it is not possible to estimate ρ and β_m from independent data, we may still be able to infer them simultaneously, for example assuming a model for ρ as a function of composition, pressure and temperature (e.g. Corsaro and Pompilio, 2004). From eq. 12 and considering the definition of β_m, we find:

$$\frac{\delta M}{\delta V} = \frac{4\mu}{3} \frac{\delta \rho}{\delta p} + \rho, \tag{15}$$

which gives an implicit equation for the density of the involved fluid. Eq. 15 is simple to solve for bubble-free magma because both density and compressibility are roughly constant for a wide range of pressures, but less straightforward if bubbles are expected to form at the depths/pressures involved. It requires a constitutive equation, $\rho = \rho(p)$; this may be complicated if the nature of the fluid involved is not known. When dealing with volatile-rich magmas or with hydrothermal fluids, or with any magmas at shallow depths, which are generally bubble-rich, the left hand side term may be very sensitive to small pressure variations, which is one of the reasons why important gravity changes may develop without corresponding ground deformation.

6.3 Generalisation to ellipsoidal geometries

We now derive equations similar to those above, except that they will be in implicit form, for more general (ellipsoidal) deformation source shapes. We consider an ellipsoidal reservoir, with one vertical axis, centered at coordinates $(0, 0, d)$, where d is depth. The surface uplift u_z at an arbitrary point (x, y) on the surface is a function of the ellipsoid's semiaxes, a, b, and c, of pressure change δp, of depth and strike of the source d and θ, and of the elastic parameters of the medium:

$$u_z(x, y) = \frac{\delta p}{\mu} f(x, y, a, b, c, d, \theta, \nu), \tag{16}$$

where the function f is obtained through combining the elastic half-space displacement Green's functions from Mindlin (1936) with the Eshelby (1957) ellipsoidal inclusion model (see also Davis, 1986). Here we assume again that the reservoir's depth is very large compared to its size (that is $d \gg \max\{a, b, c\}$) and use the Davis (1986) point-source solution to simulate the deformation field associated with pressurized ellipsoidal cavities (see also Nikkhoo et al., 2017). By using S_{iijj} terms from the Eshelby (1957) shape tensor the volume change of the pressurized ellipsoidal cavity can be calculated through

$$\delta V = \frac{\delta p V}{3K} \left(-\mathbf{J^T S_u^{-1} J} - 3\right), \tag{17}$$

where $\mathbf{J} = \begin{pmatrix} 1 & 1 & 1 \end{pmatrix}^T$, $K = \frac{2\mu(1+\nu)}{3(1-2\nu)}$ is the bulk modulus and

$$\mathbf{S_u} = \begin{pmatrix} S_{1111} - 1 & S_{1122} & S_{1133} \\ S_{2211} & S_{2222} - 1 & S_{2233} \\ S_{3311} & S_{3322} & S_{3333} - 1 \end{pmatrix}.$$

The S_{iijj} terms are nonlinear functions of the cavity semi-axes a, b and c and Poisson's ratio ν (see Amoruso and Crescentini, 2009; Segall, 2010). Note that the term $\mathbf{J^T S_u^{-1} J}$ in eq. 17 is the sum of the elements of ${\mathbf{S_u}}^{-1}$.

By using eq. 17 we can express the compressibility of a pressurized ellipsoidal cavity, β_c^{ell}, as a function of its shape and the bulk modulus, that is

$$\beta_c^{\text{ell}} = \frac{1}{V}\frac{\delta V}{\delta p} = \frac{1}{3K}\left(-\mathbf{J^T S_u^{-1} J} - 3\right). \tag{18}$$

The gravity changes due to the surface mass redistribution, Δg_{SL}, and perturbed density field, Δg_{DF}, caused by the pressurization of a ellipsoidal cavity, no longer cancel out (see Currenti et al., 2007; Trasatti and Bonafede, 2008). Thus, to evaluate Δg_{SL} and Δg_{DF} associated with the pressurized ellipsoidal cavity, we first find the equivalent CDM to the cavity (Nikkhoo et al., 2017) and then apply the Okubo (1991, 1992) solution to the three RDs that form the CDM. Superposing the gravity changes from all three RDs yields the solution for the CDM and hence, the ellipsoidal cavity.

6.4 Scenarios for Mt. Etna and other volcanoes

In this section we carry out calculations of the quantities presented above with the aim of answering the question: What gravity change could we expect for different plausible scenarios involving no detected deformation on the Earth surface?

We consider an intrusion of magma into a reservoir according to different scenarios: different reservoir shape (sphere, prolate ellipsoid, oblate ellipsoid, Tab. 1), different reservoir depths (Tabs. 2 and 3) and different degree of vesicularity for the magma (bubble-poor, intermediate and bubble-rich, Tabs. 1, 2 and 3). In order to keep the model general and dependent on very few parameters, we do not choose a specific composition, nor consider a full model where vesicularity depends on pressure and temperature. We just fix p and T and consider three representative values for the vesicularity, χ, that is 0.001, 0.005, 0.02. We then calculate the magma density, ρ, for a batch of magma of mass M and volume V, as the sum of the densities of its gas and melt phase weighted by the respective mass fractions:

$$\frac{1}{\rho} = \frac{V}{M} = \frac{V_g}{M_g}\frac{M_g}{M} + \frac{V_l}{M_l}\frac{M_l}{M} = \left(\frac{\chi RT}{M_{\text{mol}} p} + \frac{1-\chi}{\rho_l(1+\beta_l(p-p_0))}\right), \tag{19}$$

(see Tabs. 1, 2 and 3 for numerical values) where $\chi = M_g/M$ is the mass fraction in gas phase, R is the gas constant, T is absolute temperature, M_{mol} is the average molar mass of the gas phase, p_0 is a reference pressure, ρ_l and β_l are the density and the compressibility of the melt phase at pressure p_0, respectively. By using eq. 9 we derive magma compressibility for this density:

$$\beta_m = \rho \left(\frac{\chi RT}{M_{\mathrm{mol}} p^2} + \frac{(1-\chi)\beta_l}{\rho_l (1+\beta_l (p-p_0))^2} \right). \tag{20}$$

Next, for the different reservoir geometry and depth and host rock rigidity scenarios, we derive overpressure and volume change that would produce max 1 cm uplift (here taken as the maximum value that would be masked by GNSS uncertainties). Finally, we calculate the expected gravity change above the reservoir for each vesicularity value.

In the calculations we have used $\rho_{\mathrm{rock}} = 2670\,\mathrm{kg\,m^{-3}}$, $g = 9.8\,\mathrm{m\,s^{-2}}$, $\nu = 0.25$, $p = \rho_{\mathrm{rock}} g d$, $T = 1470\,\mathrm{K}$, $M_{\mathrm{mol}} = 0.025\,\mathrm{kg}$, $\rho_{\mathrm{l}} = 2670\,\mathrm{kg\,m^{-3}}$, $\beta_l = 0.2\,\mathrm{GPa^{-1}}$.

Based on our calculations shown in Tabs. 1, 2 and 3, we conclude that measurable gravity changes (a few μGal) may occur for ground deformation with $u_z < 1\,\mathrm{cm}$. The following factors promote larger gravity changes:

1. Larger magma compressibility (and thus larger r_V), see results for different columns in all tables. Note that this might imply a large volume fraction of the magma as a gas phase (see magma densities and gas volume fraction).

2. Larger rigidity of the host rock (thus larger r_V), see e.g. result for Case B compared with Case A. This can produce the same effect as above, while maintaining low magma compressibility. Overpressure will increase proportionally to maintain the same ground vertical displacement.

3. Vertically elongated reservoirs, as they are less efficient in generating vertical displacement, see Case C compared to Cases B and D.

A different source depth has a complex effect because it changes the mass fraction in gas phase, the rock elastic parameters around the source (generally higher shear and bulk modulus and lower porosity for deeper layers), the distance of the mass to the surface and the amount of pressure needed to achieve the same 1 cm displacement on the surface.

Table 1: Calculations for a reservoir of varying shape at 3 km depth.

Quantity	Explanation	Unit	Degassed	Intermediate	Gas-rich
Magma properties					
χ	Mass fraction in gas phase	—	0.001	0.005	0.02
ρ	Magma density	$\mathrm{kg\,m^{-3}}$	2630	2483	2050
V_g/V	Volume fraction in gas phase	—	0.0162	0.0761	0.251
β_m	Magma compressibility	$\mathrm{GPa^{-1}}$	0.403	1.15	3.34
Case A: Sphere					
$r = 620\,\mathrm{m},\ \mu = 1\,\mathrm{GPa},\ \beta_c = 0.750\,\mathrm{GPa^{-1}},\ \delta p = 0.504\,\mathrm{MPa},\ \delta V = 0.38 \times 10^6\,\mathrm{m^3}$					
r_V	See eq. 13	—	1.5	2.5	5.3
ΔV_β	Volume of intruded material	$1 \times 10^6\,\mathrm{m^3}$	0.58	0.95	2.03
ΔM	Mass of intruded material	$1 \times 10^9\,\mathrm{kg}$	1.53	2.37	4.17
$\Delta g - \Delta g_{\mathrm{FA}}$	Residual gravity change	µGal	1.14	1.75	3.09
Δg	Gravity change	µGal	-2.00	-1.4	-0.04
Case B: Sphere					
$r = 620\,\mathrm{m},\ \mu = 2\,\mathrm{GPa},\ \beta_c = 0.375\,\mathrm{GPa^{-1}},\ \delta p = 1.01\,\mathrm{MPa},\ \delta V = 0.38 \times 10^6\,\mathrm{m^3}$					
r_V		—	2.07	4.08	9.92
ΔV_β		$1 \times 10^6\,\mathrm{m^3}$	0.782	1.54	3.74
ΔM		$1 \times 10^9\,\mathrm{kg}$	2.06	3.81	7.63
$\Delta g - \Delta g_{\mathrm{FA}}$		µGal	1.52	2.83	5.66
Δg		µGal	-1.56	-0.26	2.57
Case C: Prolate ellipsoid					
$a = b = c/2 = 310\,\mathrm{m},\ \mu = 2\,\mathrm{GPa},\ \beta_c = 0.410\,\mathrm{GPa^{-1}},\ \delta p = 8.28\,\mathrm{MPa},\ \delta V = 0.848 \times 10^6\,\mathrm{m^3}$					
r_V		—	1.98	3.82	9.15
ΔV_β		$1 \times 10^6\,\mathrm{m^3}$	1.68	3.24	7.76
ΔM		$1 \times 10^9\,\mathrm{kg}$	4.42	8.02	15.8
$\Delta g - \Delta g_{\mathrm{FA}}$		µGal	2.07	4.75	10.5
Δg		µGal	-1.01	1.66	7.46
Case D: Oblate ellipsoid					
$a = b = 2c = 620\,\mathrm{m},\ \mu = 2\,\mathrm{GPa},\ \beta_c = 0.457\,\mathrm{GPa^{-1}},\ \delta p = 0.913\,\mathrm{MPa},\ \delta V = 0.208 \times 10^6\,\mathrm{m^3}$					
r_V		—	1.88	3.53	8.32
ΔV_β		$1 \times 10^6\,\mathrm{m^3}$	0.392	0.734	1.73
ΔM		$1 \times 10^9\,\mathrm{kg}$	1.03	1.82	3.54
$\Delta g - \Delta g_{\mathrm{FA}}$		µGal	1.27	1.86	3.13
Δg		µGal	-1.81	-1.23	0.34

Table 2: Calculations for a spherical reservoir at 2 km depth.

Quantity	Unit	Degassed	Intermediate	Gas-rich
		Magma properties		
χ	—	0.001	0.005	0.02
ρ	$\mathrm{kg\,m^{-3}}$	2608	2388	1814
V_g/V	—	0.0240	0.110	0.334
β_m	$\mathrm{GPa^{-1}}$	0.655	2.28	6.52
		Sphere		
$r = 620\,\mathrm{m}$, $\mu = 1\,\mathrm{GPa}$, $\beta_c = 0.750\,\mathrm{GPa^{-1}}$, $\delta p = 0.224\,\mathrm{MPa}$, $\delta V = 0.168 \times 10^6\,\mathrm{m^3}$				
r_V	—	1.87	4.04	9.69
ΔV_β	$1 \times 10^6\,\mathrm{m^3}$	0.314	0.677	1.62
ΔM	$1 \times 10^9\,\mathrm{kg}$	0.818	1.62	2.95
$\Delta g - \Delta g_{\mathrm{FA}}$	µGal	1.37	2.70	4.92
Δg	µGal	-1.72	-0.388	1.83

Table 3: Calculations for a spherical reservoir at 6 km depth.

Quantity	Unit	Degassed	Intermediate	Gas-rich
		Magma properties		
χ	—	0.001	0.005	0.02
ρ	$\mathrm{kg\,m^{-3}}$	2651	2577	2334
V_g/V	—	0.00814	0.0396	0.143
β_m	$\mathrm{GPa^{-1}}$	0.250	0.444	1.08
		Sphere		
$r = 620\,\mathrm{m}$, $\mu = 1\,\mathrm{GPa}$, $\beta_c = 0.750\,\mathrm{GPa^{-1}}$, $\delta p = 2.01\,\mathrm{MPa}$, $\delta V = 1.51 \times 10^6\,\mathrm{m^3}$				
r_V	—	1.33	1.59	2.45
ΔV_β	$1 \times 10^6\,\mathrm{m^3}$	2.01	2.40	3.69
ΔM	$1 \times 10^9\,\mathrm{kg}$	5.33	6.19	8.61
$\Delta g - \Delta g_{\mathrm{FA}}$	µGal	0.988	1.15	1.60
Δg	µGal	-2.10	-1.94	-1.49

7 Conduits

Some volcanic eruptions occur from established conduits, often located at the summit of a volcanic edifice, or from newly formed fissures resulting from a dike intersecting the Earth's surface during propagation. Magma flows through the old or new conduit, sometimes modifying it by eroding its walls, or plugging their thinner parts when cooling. Observations show that the cross-section of both long-lived and newly-formed conduits may have a range of aspect ratios, from cylindrical to dike-like. This applies to volcanoes of all magma compositions. At basaltic volcanoes such as Etna, the summit craters may top conduits close to cylindrical, while dike eruptions cause sheet-like conduits to form. At andesitic and silicic volcanoes, eroded domes in the field are observed to be fed both by cylindrical or dike-like conduits (Costa et al., 2007, and references therein). Mechanically, the two end-members represented by cylinders and dike-like conduits, behave very differently, with implications on the expected gravity change. Cylinders are rather incompressible shapes, meaning that large pressure variations do not lead to significant radius changes. In contrast, dike-like conduits respond to pressure changes by increasing significantly their opening. This can lead to different gravity changes during the phases preceding lava fountains or Strombolian activity, due both to a different contribution of volumetric strain induced in the edifice and to the way magma is accommodated in the conduit. Here, we present the model developed by Kazama et al. (2015) and Okubo (2020), and extend it to conduits with elliptical cross-section as well as considering magma compressibility.

7.1 Previous conduit models

We closely follow Kazama et al. (2015) and Okubo (2020) and consider magma rising in an open conduit. We simulate the conduit as a vertical open pipe of radius $a_{\rm pipe}$ that is linked to and fed by a pressurized spherical reservoir of radius $a_{\rm sph}$ embedded at depth $D_{\rm sph}$ in an elastic half-space of rigidity μ (Fig. 11).

The pipe is initially filled with magma up to an elevation of $H_{\rm head}$. When a volume of magma $\Delta V_{\rm inflow}$ of density ρ is supplied to the chamber from below, a uniform pressure change δp is expected in the sphere and most of the pipe. In the newly filled portion of the pipe, the pressure linearly decreases with the elevation. The model ignores the compressibility of the magma, so that the inflow volume is equal to the sum of: 1) volume changes in the pipe due to additional magma height, $\delta V_{\rm head}$, 2) pipe expansion, $\delta V_{\rm pipe}$, and 3) volume change in the sphere, $\delta V_{\rm sph}$ (Fig. 11), as

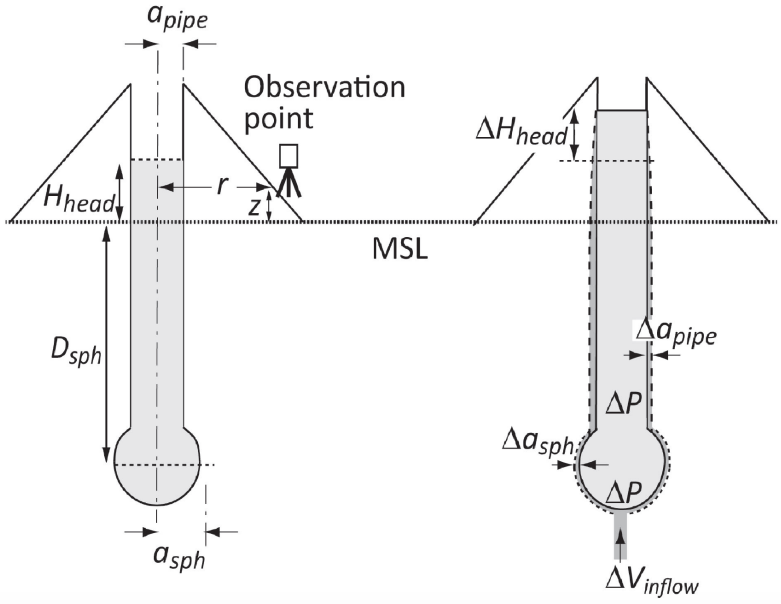

Figure 11: An open conduit coupled to a magma chamber modeled as a cylindrical pipe linked to a spherical pressure source. Left: Reference state. Right: When magma is supplied to the magma chamber, the resulting excess pressure causes elastic deformation of the pipe and sphere along with the rising magma head. Fig. 10 from Okubo (2020)

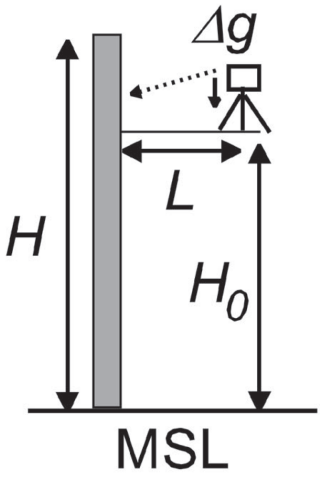

Figure 12: The line mass model used to calculate the magma head elevation. A gravimeter is located at an elevation H_0 above the MSL. The horizontal distance from the conduit to the gravimeter is L. Fig. 12b from Okubo (2020)

follows

$$\Delta V_{\text{inflow}} = \delta V_{\text{head}} + \delta V_{\text{pipe}} + \delta V_{\text{sph}} \tag{21}$$

Specifically:

$$\delta V_{\text{head}} = \pi a_{\text{pipe}}^2 \Delta H_{\text{head}} \tag{22}$$

$$\delta V_{\text{pipe}} = 2\pi a_{\text{pipe}} \delta a_{\text{pipe}} (D_{\text{sph}} + H_{\text{head}}) \tag{23}$$

$$\delta V_{\text{sph}} = 4\pi a_{\text{sph}}^2 \delta a_{\text{sph}}. \tag{24}$$

$\delta p = \rho g \Delta H_{\text{head}}$ is the pressure change. The radial expansions of the pipe and sphere are given by Bonaccorso and Davis (1999) and Yamakawa (1955) as:

$$\delta a_{\text{pipe}} = \frac{a_{\text{pipe}} \delta p}{\mu} \tag{25}$$

$$\delta a_{\text{sph}} = \frac{a_{\text{sph}} \delta p}{4\mu} \tag{26}$$

Assuming parameters appropriate for Asama volcano, as in Okubo (2020), $a_{\text{pipe}} = 70\,\text{m}$, $a_{\text{sph}} = 500\,\text{m}$, $D_{\text{sph}} = 5000\,\text{m}$, $H_{\text{head}} = 400\,\text{m}$, and $\sqrt{\mu/\rho} = 2500\,\text{m s}^{-1}$, one obtains that most of the mass goes to raise the magma head:

$$\frac{\delta V_{\text{head}}}{\delta V_{\text{inflow}}} = 0.946, \quad \frac{\delta V_{\text{pipe}}}{\delta V_{\text{inflow}}} = 0.016, \quad \frac{\delta V_{\text{sph}}}{\delta V_{\text{inflow}}} = 0.038.$$

It follows that the gravity change for the open conduit system is primarily governed by the direct attraction from the raised mass in the conduit. As the magma head rises above the observation point toward the vent (Fig. 11), the magma in the conduit attracts the gravimeter upward, resulting in a gravity decrease.

If the radius of the conduit is much smaller than the horizontal distance between the conduit and the observation point, the attraction of magma Δg can be calculated using a line mass model:

$$\Delta g(H(t)) = \pi G \rho a^2 \phi \left(\frac{1}{\sqrt{L^2 - (H(t) - H_0)^2}} - \frac{1}{L} \right) + \Delta g_0 \tag{27}$$

where $\Delta g_0 = \Delta g(H(t) = H_0)$, $H(t)$ is the height of the magma column above the mean sea level at time t, H_0 and l are the height and the horizontal distance of the gravity station (Fig. 12).

Parameters for Mt. Etna corresponding to a magma reservoir at sea level would be: $a_{\text{pipe}} = 25\,\text{m}$, $a_{\text{sph}} = 500\,\text{m}$, $D_{\text{sph}} = 3000\,\text{m}$, $H_{\text{head}} = 300\,\text{m}$, and $\sqrt{\mu/\rho} = 2500\,\text{m s}^{-1}$; using these numbers we have

$$\frac{\delta V_{\text{head}}}{\delta V_{\text{inflow}}} = 0.752, \quad \frac{\delta V_{\text{pipe}}}{\delta V_{\text{inflow}}} = 0.008, \quad \frac{\delta V_{\text{sph}}}{\delta V_{\text{inflow}}} = 0.241,$$

which leads to the conclusion that still most of the inflow into the reservoir goes to raise the magma level in the conduit. Thus eq. 27 is adequate, under the aforementioned assumptions, to model the phases preceding eruptions. For this set of parameters the contribution from the spherical magma chamber is significant and must be considered in the calculations. However, most of the inferred reservoirs at Mt. Etna are vertically elongated ellipsoids and thus, a model including an ellipsoidal magma reservoir would be desirable.

7.2 Extension to ellipsoidal reservoirs and compressible magma

We now generalise the model by considering: 1) ellipsoidal shape for the magma reservoir feeding the conduit, and 2) magma compressibility. Note that because eq. 21 assumes that magma is incompressible, it cannot be used here. Instead, the redistribution of magma in the reservoir and conduit needs to be calculated by using a mass balance equation (see Rivalta and Segall, 2008).

Again, a pipe with circular cross-section is initially filled with magma up to an elevation of $H_{\rm head}$. When a volume of magma $\Delta V_{\rm inflow}$ of density ρ is supplied to the ellipsoidal reservoir from below, a uniform pressure change δp is expected in the ellipsoid and most of the pipe. Now we do not ignore the compressibility of the magma, so that the inflow volume does not simply correspond to the sum of volume changes in the pipe due to additional magma height, $\delta V_{\rm head}$, pipe expansion, $\delta V_{\rm pipe}$, and volume change in the ellipsoidal chamber, $\delta V_{\rm ell}$ (Fig. 11), because compression of the magma previously stored in the pipe and in the chamber will accommodate some of the infill. Instead, we call $\Delta V_{\rm pipe}$ and $\Delta V_{\rm ell}$ the portion of infill volume that will be redistributed into the pipe and the ellipsoid, respectively. These volumes can be related to the volume changes they cause as follows:

$$\Delta V_{\rm ell} = r_V^{\rm ell} \delta V_{\rm ell}, \tag{28}$$

where $\delta V_{\rm ell}$ is the ellipsoid volume change from eq. 17 and the ratio $r_V^{\rm ell}$ is derived through substituting eq. 18 in eq. 13 as

$$r_V^{\rm ell} = 1 + \frac{\beta_m}{\beta_c^{\rm ell}}. \tag{29}$$

Similarly, for the open conduit we have

$$\Delta V_{\rm pipe} = r_V^{\rm pipe} \delta V_{\rm pipe}, \tag{30}$$

and

$$r_V^{\rm pipe} = 1 + \frac{\beta_m}{\beta_c^{\rm pipe}}, \tag{31}$$

where $\delta V_{\rm pipe}$ is the conduit volume change from eq. 24. The mathematical model for an open conduit is substantially different from an elongated pressurized ellipsoid, thus, here eq. 18 cannot be used to calculate $\beta_c^{\rm pipe}$. In this case we substitute $\delta V_{\rm pipe}$ from eq. 24, $\delta a_{\rm pipe}$ from eq. 26 and $V_{\rm pipe} = \pi a_{\rm pipe}^2 h_{\rm pipe}$ in eq. 10 and calculate $r_V^{\rm pipe}$ as

$$\beta_c^{\rm pipe} = \frac{2}{\mu}. \tag{32}$$

Magma density in the pipe may be much lower than in the ellipsoid due to expected larger vesiculation near the magma head where pressure gets closer to the atmospheric pressure. We indicate with $\rho_{\rm ell}$ and $\beta_m^{\rm ell}$ the magma density and compressibility in the ellipsoid, respectively, and with $\rho_{\rm pipe}$ and $\beta_m^{\rm pipe}$ the magma density and compressibility in the pipe, respectively. Thus, instead of a volume balance, we proceed with a mass balance:

$$M_{\rm inflow} = \delta M_{\rm head} + \delta M_{\rm pipe} + \delta M_{\rm ell}, \tag{33}$$

where

$$\delta M_{\rm head} = \rho_{\rm pipe} \Delta V_{\rm head}, \tag{34}$$

$$\delta M_{\rm pipe} = \rho_{\rm pipe} r_V^{\rm pipe} \delta V_{\rm pipe}, \tag{35}$$

$$\delta M_{\rm ell} = \rho_{\rm ell} r_V^{\rm ell} \delta V_{\rm ell}, \tag{36}$$

are the amount of mass distributed in the magma head, the conduit and the reservoir, respectively. Furthermore, by using eq. 8 we have

$$\delta M_{\rm head} = \pi a_{\rm pipe}^2 g^{-1} \delta p, \tag{37}$$

$$\delta M_{\rm pipe} = \pi a_{\rm pipe}^2 \rho_{\rm pipe} (\beta_m^{\rm pipe} + \beta_c^{\rm pipe})(D_{\rm ell} + H_{\rm head} - c)\delta p, \tag{38}$$

$$\delta M_{\rm ell} = (4/3)\pi abc \rho_{\rm ell} (\beta_m^{\rm ell} + \beta_c^{\rm ell})\delta p. \tag{39}$$

As an example, we repeat the calculation for Mt. Etna. Again, we assume a spherical reservoir at sea level ($D_{\rm sph} = 3000\,{\rm m}$) with a radius of 500 m, a shear modulus of $\mu = 16.875\,{\rm GPa}$, a pipe radius of $a_{\rm pipe} = 25\,{\rm m}$, a magma head height of $H_{\rm head} = 300\,{\rm m}$ above the free surface for the ground deformation calculations. We consider the "effective" free surface to be at 3000 m elevation. We calculate the total magma column height as $H_{\rm head} + D_{\rm sph} - a_{\rm sph}$, where we remove an amount equal to the radius of the reservoir from the calculation; this is different from Okubo (2020), who ignored the radius of the sphere and considered only $H_{\rm head} + D_{\rm sph}$ (see eq. 24). We calculate the magma densities and compressibilities at the conduit and reservoir levels using eqs. 19 and 20, respectively. We take $\chi = 0.001$ assuming that magma at such shallow levels is rather degassed. Eq. 19 also assumes that the mass fraction in gas phase is constant. This implies that the bubbles nucleated between the reservoir and conduit, if any, are efficiently released; thus, the volume fraction of gas increases just by expansion driven by decompression. For the conduit we take a pressure corresponding to a level half-way along it from the top of the head, so that we have depth 1400 m and $p = 36.6\,{\rm MPa}$; for the reservoir we have depth from the top of the magma column of 3300 m and $p = 86.3\,{\rm MPa}$. For the pipe we obtain $\rho_{\rm pipe} = 2582\,{\rm kg\,m^{-3}}$, $\beta_m^{\rm pipe} = 1.12\,{\rm GPa^{-1}}$, gas volume fraction is 0.0340, $\beta_c^{\rm pipe} = 0.119\,{\rm GPa^{-1}}$. For the reservoir we obtain $\rho_{\rm sph} = 2633\,{\rm kg\,m^{-3}}$, $\beta_m^{\rm sph} = 0.367\,{\rm GPa^{-1}}$, gas volume fraction is 0.0147, $\beta_c^{\rm sph} = 0.0444\,{\rm GPa^{-1}}$. This returns:

$$\frac{\delta M_{\rm head}}{M_{\rm inflow}} = 0.14, \quad \frac{\delta M_{\rm pipe}}{M_{\rm inflow}} = 0.026, \quad \frac{\delta M_{\rm sph}}{M_{\rm inflow}} = 0.83.$$

An important observation in the result is that compared to the previous example without magma compressibility the mass redistribution is reversed.

As a final example, we repeat the calculation for a shallower ellipsoidal reservoir at Mt. Etna. We assume a vertical prolate magma reservoir with minor semiaxes $a = b = 300\,{\rm m}$ and major semiaxis $c = 600\,{\rm m}$. We assume the shear modulus is $\mu = 1\,{\rm GPa}$, the pipe radius is $a_{\rm pipe} = 25\,{\rm m}$, the depth of the centre of the ellipsoidal reservoir is $D_{\rm ell} = 1200\,{\rm m}$, the head height $H_{\rm head} = 300\,{\rm m}$ above the free surface for the ground deformation calculations. We consider the head to be located at 300 m below the summit, this way the "effective" free surface will be at 2700 m elevation. We calculate the total magma column height as $H_{\rm head} + D_{\rm ell} - c$. We calculate the magma densities and compressibilities at the conduit and reservoir levels using eqs. 19 and 20, respectively. We take $\chi = 0.001$. For the conduit we take a pressure corresponding to a level half-way along it from the top of the head, so that we have depth 600 m and $p = 15.7\,{\rm MPa}$; for the reservoir we have depth 1500 m and $p = 39.2\,{\rm MPa}$. For the pipe we obtain $\rho_{\rm pipe} = 2470\,{\rm kg\,m^{-3}}$, $\beta_m^{\rm pipe} = 5.02\,{\rm GPa^{-1}}$, gas volume fraction is 0.0759, $\beta_c^{\rm pipe} = 2\,{\rm GPa^{-1}}$. For the ellipsoid we obtain $\rho_{\rm ell} = 2588\,{\rm kg\,m^{-3}}$, $\beta_m^{\rm ell} = 1.00\,{\rm GPa^{-1}}$, gas volume fraction is 0.0318, $\beta_c^{\rm ell} = 0.820\,{\rm GPa^{-1}}$. This returns:

$$\frac{\delta M_{\rm head}}{M_{\rm inflow}} = 0.081, \quad \frac{\delta M_{\rm pipe}}{M_{\rm inflow}} = 0.026, \quad \frac{\delta M_{\rm ell}}{M_{\rm inflow}} = 0.894.$$

Thus, with this model and this particular choice of parameters, the magma reservoir takes the largest share of the mass inflow. Obviously, the magma reservoir takes up more magma mass if it is larger and the conduit thinner and shorter. Here, this occurs in spite of larger compressibility in the pipe. Thus, these factors need to be estimated with care. Gravity changes acquired during the phases preceding eruptions may help constraining these geometrical factors, assuming the geometry remains stable for at least some eruptions.

8 Final remarks

In this report, we extend available analytical and semi-analytical solutions to treat the coupled effects of deformation and gravity change caused by pressurized ellipsoidal cavities at volcanoes. Parts of these results and MATLAB codes for computation will be published as a peer-reviewed article (Nikkhoo and Rivalta, 2020 in preparation).

Our findings can be summarised as follows:

1. As previously pointed out (e.g. Okubo, 1991, 1992), in order to correctly estimate gravity changes at volcanoes we need to consider the vertical displacements of the gravity stations (free-air gradient contribution, which in general dominates gravity changes) and deformation of the medium (both due to subsurface volumetric strains and to mass redistribution at the Earth's surface). This requires a joint analysis of deformation and gravity changes.

2. The shape of the deformation source affects the gravity change in a way that often cannot be neglected. This occurs because for non-spherical sources the induced subsurface volumetric strains and mass redistribution at the Earth's surface cause significant gravity changes (Bonafede and Mazzanti, 1998; Currenti et al., 2007; Trasatti and Bonafede, 2008). Moreover, ellipsoidal reservoirs, except for tabular or near tabular, are rather "incompressible" and "hide" some of the intruded or extruded fluid volume by compressing or decompressing the previously contained fluid. In this context, spherical reservoirs represent the least compressible shapes. Compressibility effects, depending on the specific scenario, may be large enough to bias estimates of magma density from gravity observations. As this may lead to incorrect interpretations with implications for hazard assessment, it is very important to include compressibility in the calculations. This issue has been already mentioned in textbooks (Dzurisin, 2006; Segall, 2010) and a number of studies considering gravity change (e.g. Johnson, 1992; Currenti, 2014) and deformation (e.g. Johnson et al., 2000; Rivalta and Segall, 2008; Hreinsdóttir et al., 2014; Nikkhoo et al., 2017). However, the issue is still mostly neglected when interpreting observed gravity changes. Here, we outline how magma and reservoir compressibility can be included in the calculations.

3. Although many studies exist that use source shapes beyond spherical, cylindrical and sheet-like, these studies have been mostly carried out by using numerical methods providing results only for specific cases, without exploring the variability that can occur in nature. These are not widely usable by the community. We have developed codes that will provide a much wider community with the tools to rigorously perform forward simulations of gravity changes and to conduct comprehensive joint inversions of gravity change and deformation data on a commonly available personal computer.

4. Here we do not directly address layering. Displacing vertically the interfaces of a layered medium due to source pressurisation may also lead to measurable gravity changes and should be included when possible (Bonafede and Mazzanti, 1998; Trasatti and Bonafede, 2008; Currenti, 2014; Segall, 2010). This can be done in the framework we propose by using point sources in layered media (Amoruso et al., 2008).

5. Similarly, our point-source approach can potentially be applied to problems involving complex rheologies such as viscoelastic problems, provided that efficient analytical or semi-analytical solutions associated with these rheologies exist.

References

Aloisi, M., Bonaccorso, A., Cannavò, F., Currenti, G., and Gambino, S. (2020). The 24 december 2018 eruptive intrusion at etna volcano as revealed by multidisciplinary continuous deformation networks (cgps, borehole strainmeters and tiltmeters). *Journal of Geophysical Research: Solid Earth*, 125(8):e2019JB019117.

Amoruso, A. and Crescentini, L. (2009). Shape and volume change of pressurized ellipsoidal cavities from deformation and seismic data. *Journal of Geophysical Research: Solid Earth*, 114(B2).

Amoruso, A., Crescentini, L., and Berrino, G. (2008). Simultaneous inversion of deformation and gravity changes in a horizontally layered half-space: evidences for magma intrusion during the 1982–1984 unrest at campi flegrei caldera (italy). *Earth and Planetary Science Letters*, 272(1-2):181–188.

Bagnardi, M., Poland, M. P., Carbone, D., Baker, S., Battaglia, M., and Amelung, F. (2014). Gravity changes and deformation at kīlauea volcano, hawaii, associated with summit eruptive activity, 2009–2012. *Journal of Geophysical Research: Solid Earth*, 119(9):7288–7305.

Beauducel, F. (2012). Okubo: Gravity change due to shear and tensile faults. http://www.ipgp.fr/ beaudu/matlab.html. MATLAB code.

Bonaccorso, A., Aoki, Y., and Rivalta, E. (2017). Dike propagation energy balance from deformation modeling and seismic release. *Geophysical Research Letters*, 44(11):5486–5494.

Bonaccorso, A., Cianetti, S., Giunchi, C., Trasatti, E., Bonafede, M., and Boschi, E. (2005). Analytical and 3-d numerical modelling of mt. etna (italy) volcano inflation. *Geophysical Journal International*, 163(2):852–862.

Bonaccorso, A. and Davis, P. M. (1999). Models of ground deformation from vertical volcanic conduits with application to eruptions of mount st. helens and mount etna. *Journal of Geophysical Research: Solid Earth*, 104(B5):10531–10542.

Bonafede, M. and Mazzanti, M. (1998). Modelling gravity variations consistent with ground deformation in the campi flegrei caldera (italy). *Journal of Volcanology and Geothermal Research*, 81(1-2):137–157.

Branca, S. (2003). Geological and geomorphological evolution of the etna volcano ne flank and relationships between lava flow invasions and erosional processes in the alcantara valley (italy). *Geomorphology*, 53(3-4):247–261.

Carbone, D., Budetta, G., and Greco, F. (2003). Bulk processes prior to the 2001 mount etna eruption, highlighted through microgravity studies. *Journal of Geophysical Research: Solid Earth*, 108(B12).

Carbone, D., Cannavó, F., Greco, F., Reineman, R., and Warburton, R. J. (2019). The benefits of using a network of superconducting gravimeters to monitor and study active volcanoes. *Journal of Geophysical Research: Solid Earth*, 124(4):4035–4050.

Carbone, D., Currenti, G., and Del Negro, C. (2008a). Multiobjective genetic algorithm inversion of ground deformation and gravity changes spanning the 1981 eruption of etna volcano. *Journal of Geophysical Research: Solid Earth*, 113(B7).

Carbone, D. and Poland, M. P. (2012). Gravity fluctuations induced by magma convection at kīlauea volcano, hawai'i. *Geology*, 40(9):803–806.

Carbone, D., Poland, M. P., Diament, M., and Greco, F. (2017). The added value of time-variable microgravimetry to the understanding of how volcanoes work. *Earth-Science Reviews*, 169:146–179.

Carbone, D., Zuccarello, L., Messina, A., Scollo, S., and Rymer, H. (2015). Balancing bulk gas accumulation and gas output before and during lava fountaining episodes at mt. etna. *Scientific reports*, 5(1):1–11.

Carbone, D., Zuccarello, L., and Saccorotti, G. (2008b). Geophysical indications of magma uprising at mt etna during the december 2005 to january 2006 non-eruptive period. *Geophysical Research Letters*, 35(6).

Chauhan, M. S., Cannavó, F., Carbone, D., and Greco, F. (2020). Insights into mount etna december 2018 eruption from joint inversion of deformation and gravity data. *Geophysical Research Letters*, 47(16):e2020GL087786.

Corsaro, R. A. and Pompilio, M. (2004). Buoyancy-controlled eruption of magmas at mt etna. *Terra Nova*, 16(1):16–22.

Costa, A., Melnik, O., and Sparks, R. (2007). Controls of conduit geometry and wallrock elasticity on lava dome eruptions. *Earth and Planetary Science Letters*, 260(1-2):137–151.

Currenti, G. (2014). Numerical evidence enabling reconciliation gravity and height changes in volcanic areas. *Geophysical Journal International*, 197(1):164–173.

Currenti, G. (2018). Viscoelastic modeling of deformation and gravity changes induced by pressurized magmatic sources. *Journal of Volcanology and Geothermal Research*, 356:264–277.

Currenti, G., Del Negro, C., and Ganci, G. (2007). Modelling of ground deformation and gravity fields using finite element method: an application to Etna volcano. *Geophysical Journal International*, 169(2):775–786.

Davis, P. M. (1986). Surface deformation due to inflation of an arbitrarily oriented triaxial ellipsoidal cavity in an elastic half-space, with reference to kilauea volcano, hawaii. *Journal of Geophysical Research: Solid Earth*, 91(B7):7429–7438.

Dzurisin, D. (2006). *Volcano deformation: new geodetic monitoring techniques*. Springer Science & Business Media.

Eggers, A. (1987). Residual gravity changes and eruption magnitudes. *Journal of Volcanology and Geothermal Research*, 33(1-3):201–216.

Eshelby, J. D. (1957). The determination of the elastic field of an ellipsoidal inclusion, and related problems. *Proceedings of the royal society of London. Series A. Mathematical and physical sciences*, 241(1226):376–396.

Gottsmann, J., Berrino, G., Rymer, H., and Williams-Jones, G. (2003). Hazard assessment during caldera unrest at the campi flegrei, italy: a contribution from gravity–height gradients. *Earth and Planetary Science Letters*, 211(3-4):295–309.

Hardt, M. and Scherbaum, F. (1994). The design of optimum networks for aftershock recordings. *Geophysical Journal International*, 117(3):716–726.

Hreinsdóttir, S., Sigmundsson, F., Roberts, M. J., Björnsson, H., Grapenthin, R., Arason, P., Árnadóttir, T., Hólmjárn, J., Geirsson, H., Bennett, R. A., et al. (2014). Volcanic plume height correlated with magma-pressure change at grímsvötn volcano, iceland. *Nature geoscience*, 7(3):214–218.

Jackson, M., Blundy, J., and Sparks, R. (2018). Chemical differentiation, cold storage and remobilization of magma in the earth's crust. *Nature*, 564(7736):405–409.

Johnson, D. J. (1992). Dynamics of magma storage in the summit reservoir of kilauea volcano, hawaii. *Journal of Geophysical Research: Solid Earth*, 97(B2):1807–1820.

Johnson, D. J., Eggers, A. A., Bagnardi, M., Battaglia, M., Poland, M. P., and Miklius, A. (2010). Shallow magma accumulation at kīlauea volcano, hawai 'i, revealed by microgravity surveys. *Geology*, 38(12):1139–1142.

Johnson, D. J., Sigmundsson, F., and Delaney, P. T. (2000). Comment on" volume of magma accumulation or withdrawal estimated from surface uplift or subsidence, with application to the 1960 collapse of kīlauea volcano" by pt delaney and df mctigue. *Bulletin of Volcanology*, 61(7):491–493.

Kazama, T., Okubo, S., Sugano, T., Matsumoto, S., Sun, W., Tanaka, Y., and Koyama, E. (2015). Absolute gravity change associated with magma mass movement in the conduit of asama volcano (central japan), revealed by physical modeling of hydrological gravity disturbances. *Journal of Geophysical Research: Solid Earth*, 120(2):1263–1287.

Kilbride, B. M., Edmonds, M., and Biggs, J. (2016). Observing eruptions of gas-rich compressible magmas from space. *Nature Communications*, 7(1):1–8.

Koulakov, I., Gordeev, E. I., Dobretsov, N. L., Vernikovsky, V. A., Senyukov, S., Jakovlev, A., and Jaxybulatov, K. (2013). Rapid changes in magma storage beneath the klyuchevskoy group of volcanoes inferred from time-dependent seismic tomography. *Journal of Volcanology and Geothermal Research*, 263:75–91.

Mastin, L. G., Lisowski, M., Roeloffs, E., and Beeler, N. (2009). Improved constraints on the estimated size and volatile content of the mount st. helens magma system from the 2004–2008 history of dome growth and deformation. *Geophysical Research Letters*, 36(20).

Mindlin, R. D. (1936). Force at a point in the interior of a semi-infinite solid. *physics*, 7(5):195–202.

Mogi, K. (1958). Relations between the eruptions of various volcanoes and the deformation of the ground surfaces around them. *Bulletin of the Earthquake Research Institute*, 36:99–134.

Nikkhoo, M., Rivalta, E., Connavò, F., and Carbone, D. (2020). Analytical and numerical optimal design for gravimetric networks: case study mt. etna, italy. *in preparation*.

Nikkhoo, M., Walter, T. R., Lundgren, P. R., and Prats-Iraola, P. (2017). Compound dislocation models (cdms) for volcano deformation analyses. *Geophysical Journal International*, page ggw427.

Okada, Y. (1992). Internal deformation due to shear and tensile faults in a half-space. *Bulletin of the seismological society of America*, 82(2):1018–1040.

Okubo, S. (1991). Potential and gravity changes raised by point dislocations. *Geophysical journal international*, 105(3):573–586.

Okubo, S. (1992). Gravity and potential changes due to shear and tensile faults in a half-space. *Journal of Geophysical Research: Solid Earth*, 97(B5):7137–7144.

Okubo, S. (2020). Advances in gravity analyses for studying volcanoes and earthquakes. *Proceedings of the Japan Academy, Series B*, 96(2):50–69.

Pinel, V., Carrara, A., Maccaferri, F., Rivalta, E., and Corbi, F. (2017). A two-step model for dynamical dike propagation in two dimensions: Application to the july 2001 etna eruption. *Journal of Geophysical Research: Solid Earth*, 122(2):1107–1125.

Poland, M. P., de Zeeuw-van Dalfsen, E., Bagnardi, M., and Johanson, I. A. (2019). Post-Collapse Gravity Increase at the Summit of Kīlauea Volcano, Hawai'i. *Geophysical Research Letters*, 46(24):14430–14439.

Rivalta, E. (2010). Evidence that coupling to magma chambers controls the volume history and velocity of laterally propagating intrusions. *Journal of Geophysical Research: Solid Earth*, 115(B7).

Rivalta, E., Corbi, F., Passarelli, L., Acocella, V., Davis, T., and Di Vito, M. A. (2019). Stress inversions to forecast magma pathways and eruptive vent location. *Science advances*, 5(7):eaau9784.

Rivalta, E. and Segall, P. (2008). Magma compressibility and the missing source for some dike intrusions. *Geophysical Research Letters*, 35(4).

Rymer, H. and Williams-Jones, G. (2000). Volcanic eruption prediction: Magma chamber physics from gravity and deformation measurements. *Geophysical Research Letters*, 27(16):2389–2392.

Segall, P. (2010). *Earthquake and volcano deformation*. Princeton University Press.

Sigmundsson, F., Hooper, A., Hreinsdóttir, S., Vogfjörd, K. S., Ófeigsson, B. G., Heimisson, E. R., Dumont, S., Parks, M., Spaans, K., Gudmundsson, G. B., et al. (2015). Segmented lateral dyke growth in a rifting event at bárðarbunga volcanic system, iceland. *Nature*, 517(7533):191–195.

Taisne, B. and Jaupart, C. (2009). Dike propagation through layered rocks. *Journal of Geophysical Research: Solid Earth*, 114(B9).

Thiele, S., Cruden, A., Micklethwaite, S., Bunger, A., and Köpping, J. (2020). Dyke apertures record stress accumulation during sustained volcanism. *in press*.

Trasatti, E. and Bonafede, M. (2008). Gravity changes due to overpressure sources in 3d heterogeneous media: application to campi flegrei caldera, italy. *Annals of Geophysics*.

Urbani, S., Acocella, V., Rivalta, E., and Corbi, F. (2017). Propagation and arrest of dikes under topography: Models applied to the 2014 bardarbunga (iceland) rifting event. *Geophysical Research Letters*, 44(13):6692–6701.

Walsh, J. and Rice, J. (1979). Local changes in gravity resulting from deformation. *Journal of Geophysical Research: Solid Earth*, 84(B1):165–170.

Weertman, J. (1971). Theory of water-filled crevasses in glaciers applied to vertical magma transport beneath oceanic ridges. *Journal of Geophysical Research*, 76(5):1171–1183.

Wright, T. J., Sigmundsson, F., Pagli, C., Belachew, M., Hamling, I. J., Brandsdóttir, B., Keir, D., Pedersen, R., Ayele, A., Ebinger, C., et al. (2012). Geophysical constraints on the dynamics of spreading centres from rifting episodes on land. *Nature Geoscience*, 5(4):242–250.

Yamakawa, N. (1955). On the strain produced in a semi-infinite elastic solid by an interior source of stress. *J. Seismol. Soc. Japan, Ser. 2*, 8(2):84–98.